CANCER

Atypical inflammatory kinase IKBKE phosphorylates and inactivates FoxA1 to promote liver tumorigenesis

Bing Gao[1,2]†, Xueji Wu[2]†, Lang Bu[2]†, Qiwei Jiang[2]†, Lei Wang[2], Haining Liu[1,2], Xiaomei Zhang[2], Yuanzhong Wu[3], Xiaoxing Li[1,2], Jingting Li[2], Ying Liang[4]*, Lixia Xu[2,5]*, Wei Xie[2]*, Jianping Guo[2]*

Physiologically, FoxA1 plays a key role in liver differentiation and development, and pathologically exhibits an oncogenic role in prostate and breast cancers. However, its role and upstream regulation in liver tumorigenesis remain unclear. Here, we demonstrate that FoxA1 acts as a tumor suppressor in liver cancer. Using a CRISPR-based kinome screening approach, noncanonical inflammatory kinase IKBKE has been identified to inhibit FoxA1 transcriptional activity. Notably, IKBKE directly binds to and phosphorylates FoxA1 to reduce its complex formation and DNA interaction, leading to elevated hepatocellular malignancies. Nonphosphorylated mimic *Foxa1* knock-in mice markedly delay liver tumorigenesis in hydrodynamic transfection murine models, while phospho-mimic *Foxa1* knock-in phenocopy *Foxa1* knockout mice to exhibit developmental defects and liver inflammation. Notably, *Ikbke* knockout delays diethylnitrosamine (DEN)-induced mouse liver tumor development. Together, our findings not only reveal FoxA1 as a bona fide substrate and negative nuclear effector of IKBKE in hepatocellular carcinioma (HCC) but also provide a promising strategy to target IKBEK for HCC therapy.

INTRODUCTION

Liver cancer is the fourth leading cause of cancer death in both sexes (8.2% of all cancer deaths) (*1*). It is worth noting that hepatocellular carcinoma (HCC), the most common form of liver cancer, is usually caused by excessive alcohol consumption, viral hepatitis [hepatitis B virus (HBV) and HCV)], or nonalcoholic fatty liver disease with inflammation that promotes liver fibrosis and tumorigenesis (*2*, *3*). Therefore, HCC is considered an inflammatory disease. Thus, in a murine model of carcinogen-induced HCC, inhibition of signal transducer and activator of transcription 3 (STAT3) in hepatocytes successfully blocked HCC development (*4*). In addition, proinflammatory cytokines such as interleukin-6 (IL-6) and tumor necrosis factor (TNF), which activate STAT3 and nuclear factor κB (NF-κB) signaling, respectively, play major roles in initiation and progression of HCC (*5*, *6*). Notably, inhibition of NF-κB increased hepatocyte proliferation in diethylnitrosamine (DEN)–induced and HBV surface antigen–driven HCC murine models (*7*, *8*). However, there are currently no effective strategies to combat HCC by targeting the NF-κB pathway.

The inhibitor of NF-κB kinase subunit epsilon (IKBKE) belongs to noncanonical IκB kinases. IKBKE and TNF receptor-associated factor (TANK)–binding kinase 1 (TBK1) have been reported to be involved in energy storage and inflammatory programs in the liver and adipose tissues, where abnormality of *IKBKE* contributes to obesity (*9*). In addition to regulating NF-κB (*10*) and STAT1–interferon regulatory factor 3/7 (IRF3/7)–mediated inflammatory signaling pathways (*11*), the function of IKBKE in tumorigenesis has also been decoded in many other ways. For example, IKBKE integrates with STAT3 activation to compose a cytokine signaling network in a subset of immune-activated triple-negative breast cancer (*12*), and IKBEK also promotes the phosphorylation of Yes1-associated transcriptional regulator (YAP) to alleviate the effect of YAP on cellular antiviral response (*13*), which occurs in approximately 30% patients with HCC (*14*). As an inducible kinase, *IKBKE* could be induced by various cytokines or chemokines, including phorbol 12-myristate 13-acetate (PMA) and lipopolysaccharide (LPS) (*15*, *16*). Conceivably, inflammation-related HCC would bear a high level of IKBKE; however, the function of IKBKE in HCC is still under exploration.

Hepatocyte nuclear factor 3-alpha (FoxA1), initially identified as a liver-specific transcription factor involved in hepatocyte differentiation and development (*17*), has recently attracted more attention due to its oncogenic role in tumorigenesis, especially in breast and prostate cancer settings. FoxA1 can assist estrogen receptor (ER) or androgen receptor (AR) to regulate downstream gene expression (*18*–*20*) and has been considered as an effective target for prostate cancer therapy due to its gain-of-function mutations in boosting prostate tumorigenesis (*21*). Sexual dimorphism of HCC that estrogens prevent and androgens promote liver cancer, which is largely dependent on the presence of *Foxa1* and *Foxa2* in DEN-induced HCC murine model (*22*). Recently, FoxA1 has been suggested to play potential tumor suppressor role in certain studies (*23*). Therefore, urgent efforts are desired to identify FoxA1 upstream regulators and consequently develop effective therapeutic interventions for HCC.

In conclusion, here, we initially reveal the tumor suppressor role of FoxA1 in HCC and further integrate CRISPR-based screening approach, biochemical studies, and genetic mouse models to demonstrate that accumulated IKBKE-mediated phosphorylation and inactivation of FoxA1 contribute to liver tumorigenesis, which would be efficiently alleviated by IKBKE inhibitors.

RESULTS

FoxA1 plays a tumor suppressor role in HCC

Recently, the critical role and clinical relevance of FoxA1 as an oncogene in prostate and breast cancers has been established (*18*, *21*);

[1]Center of Hepato-Pancreate-Biliary Surgery, the First Affiliated Hospital, Sun Yat-sen University, Guangzhou, Guangdong, 510275, China. [2]Institute of Precision Medicine, the First Affiliated Hospital, Sun Yat-sen University, Guangzhou, Guangdong 510275, China. [3]State Key Laboratory of Oncology in South China, Collaborative Innovation Center for Cancer Medicine, Sun Yat-sen University Cancer Center, Guangzhou, Guangdong 510060, China. [4]Department of Nephrology, Guangzhou Eighth People's Hospital, Guangzhou Medical University, Guangdong 510060, China. [5]Department of Oncology, the First Affiliated Hospital, Sun Yat-sen University, Guangzhou, Guangdong 510275, China.
*Corresponding author. Email: gz8hliangying@yeah.net (Y.L.); xulixia@mail.sysu.edu.cn (L.X.); xiew56@mail.sysu.edu.cn (W.X.); guojp6@mail.sysu.edu.cn (J.G.)
†These authors contributed equally to this work.

however, its potential role in HCC has just begun to be explored (*24*–*27*). Here, we observed that depletion of *FoxA1* dramatically enhanced hepatic cancer cell colony formation, anchorage growth (Fig. 1, A and B, and fig. S1, A to C), and tumor growth in mice (Fig. 1, C and D, and fig. S1, D to F). Depletion of *FoxA1* significantly increased HCC organoid formation (Fig. 1, E and F). Consistent with these findings, re-introduction of FoxA1 in *FoxA1*-depleted HCC cells effectively rescued FoxA1 tumor suppressor effect in impairing cell colony formation (fig. S1, G and H). These data collectively implicate a potential tumor suppressor role of FoxA1 in HCC.

However, compared to the frequent genetic alterations of *FoxA1* in the prostate cancer setting, where FoxA1 acts as an oncogene with gain-of-function mutations (more than 4%) (*21*), alterations of *FoxA1* are rarely observed in patients with HCC. In contrast, bioinformatic analysis from The Cancer Genome Atlas dataset revealed that high mRNA levels of *FoxA1* indicated a poor prognosis in patients with HCC, whereas high expression of FoxA2 or FoxA3 showed better outcomes (fig. S1I). To this end, we sought to detect FoxA1 protein levels in HCC tissues. Notably increased FoxA1 protein was observed in HCC tissues compared with paired adjacent normal tissues (fig. S1, J and K), suggesting that the mRNA and protein levels of FoxA1 did not well associated with its tumor suppressor function, suggesting that posttranslational modifications (PTMs) may play a key role in regulating the tumor suppressor of FoxA1.

IKBKE represses FoxA1 transcriptional activation

Although several PTMs of FoxA1, including acetylation, methylation, and ubiquitination, have been reported in prostate cancer (*28*–*30*), the phosphorylation modification has not been identified to affect FoxA1 function. To this end, we established a CRISPR-Cas9–based kinome screen method (Fig. 1G). For that, a reporter construct containing FoxA1-response elements (FRE) was designed, which also exhibited unexpected cross-reactivity to forkhead BOX O3 (FoxO3a), but not forkhead BOX D4 (FoxD4) and forkhead BOX P1 (FoxP1) (fig. S2A). As a result, ectopic expression of both FoxA1 and FoxO3a could notably increase the expression of green fluorescent protein (GFP) reporter gene (fig. S2B). Then, the reporter construct cells were infected with CRISPR kinase pools (Fig. 1G), and the resulting cells were subjected to the kinome screen analysis by flow cytometry–based sorting and deep sequencing methods (*31*) to identify kinases that regulate FoxA1 transcriptional activity (Fig. 1H and fig. S2, C and D).

Among the screening results, we focused on potential kinases that negatively regulate FoxA1 transcriptional activity, which may be further used as therapeutic targets. As a result, polo like kinase 3 (PLK3), AKT serine/threonine kinase 1 (AKT1), SIK family kinase 3 (SIK3), NIMA-related kinase 10 (NEK10), IKBKE, 3-phosphoinositide–dependent protein kinase 1 (PDK1), and mitogen-activated protein kinase 6 (MAPK6) are ranked in the top of repressing FoxA1 transcriptional activity (Fig. 1H). Furthermore, ectopic expression of these kinases was performed, among them, IKBKE, to a lesser extent of AKT1, was shown to readily reduce FoxA1 reporter activity (fig. S2E). To validate the function of IKBKE in regulating FoxA1, ectopic expression of wild type (WT) or constitutively active IKBKE (Myr-IKBKE) (*32*), but not TBK1 or kinase dead (DN) IKBKE-K23M, significantly decreased FoxAs (FoxA1-3) transcription activity (Fig. 1I and fig. S2, F and G). Furthermore, through transcriptomic analyses, *IKBKE* depletion-induced alterations of gene expression markedly overlapped with those derived from *FoxA1* knockdown cells (Fig. 1, J and K, and fig. S2, H and I), including cell cycle–related genes such as BUB1 mitotic checkpoint serine/threonine kinase (BUB1), cyclin D1 (CCND1), and the oncogene mesenchymal epithelial transition (MET) (Fig. 1, L and M). These findings collectively suggest that IKBKE inhibits FoxA1 transcriptional activation (Fig. 1N).

IKBKE exerts oncogenic function in HCC by repressing FoxA1

Because of the functional negative regulation of FoxA1 by IKBKE in HCC (Fig. 1, I to N), we sought to investigate the potential pathological relevance of IKBKE in HCC. Bioinformatic analyses revealed that *IKBKE* exhibited approximately 4 to 8% amplification in the HCC settings, and its expression was strongly associated with poor survival in both alcohol- and hepatitis virus–associated HCC (mainly in the male patient cohort) (fig. S3, A to C). Furthermore, immunoblot analysis implied that IKBKE was highly expressed in HCC tissues compared with adjacent normal tissues (fig. S1K). Immunohistochemistry (IHC) staining further revealed that IKBKE expression correlated with the early stage of HCC to predict poor patient outcomes (fig. S3, D to F), suggesting that IKBKE should be an early event for HCC. Similar to the oncogenic role of IKBKE in breast and other cancers (*33*), depletion of *IKBKE* significantly reduced HCC cell growth, colony formation (Fig. 2, A and B, and fig. S4A), tumor growth (Fig. 2, C to E, and fig. S4, B and C), and HCC organoid formation (Fig. 2, F and G), and impaired NF-κB and phosphatidylinositol 3-kinase (PI3K)–AKT pathways (fig. S4C). To explore the potential role of IKBKE in vivo, the chemical carcinogen DEN was used to generate a murine model of hepatocarcinogenesis. The results showed that *Ikbke* knockout (*Ikbke*$^{-/-}$) mice were resistant to DEN-induced liver inflammation (with the marker F4/80), proliferation (with the marker Ki67), and tumor formation (with the liver cancer marker CK19 and normal liver tissue marker HNF4α) compared with counterpart mice (Fig. 2, H and I, and fig. S4D), suggesting a protective effect of IKBKE on hepatocytes. Furthermore, knockdown of *FoxA1* partially rescued *IKBKE* depletion-induced cell growth inhibition (Fig. 2, J and K, and fig. S4, E and F), accompanied with increased IKBKE substrates such as pS473-AKT and phosphor–NF-κB inhibitor alpha (p-Iκ-Bα), suggesting that FoxA1 likely defects the oncogenic role of IKBKE in HCC.

IKBKE directly phosphorylates FoxA1

To investigate the underlying mechanism of IKBKE in impairing FoxA1 transcriptional activity, we observed the stable interaction of IKBKE and FoxA1 at both exogenous and endogenous levels (Fig. 3A and fig. S4, G and H). Furthermore, the Forkhead (FH) domain of FoxA1, the major part of FoxA1 binding to DNA, was narrowed to specifically interact with IKBKE (Fig. 3B). While among FoxA family proteins, FoxA2 displayed a relatively lower binding affinity to IKBKE (fig. S4H). To disclose the potential role of IKBKE in regulating FoxA1, we hypothesized that IKBKE could directly phosphorylate FoxA1 to inhibit its activity. To this end, a band shift of FoxA1, a common indicator of protein phosphorylation, was observed upon enforcing IKBKE expression, which could be reduced by addition of lambda phosphatase (λ-phosphatase) (fig. S5A). Similar results were observed by using a phospho-tag approach, where Myr-IKBKE enhanced FoxA1 phosphorylation (fig. S5B). Furthermore, in vitro kinase assays revealed that IKBKE directly phosphorylated FoxA1 (fig. S5C).

To determine the phosphorylation residues of FoxA1 by IKBKE, we performed mass spectrometry analysis and observed that the S174 and S177 sites, located in the FH domain of FoxA1, were possibly

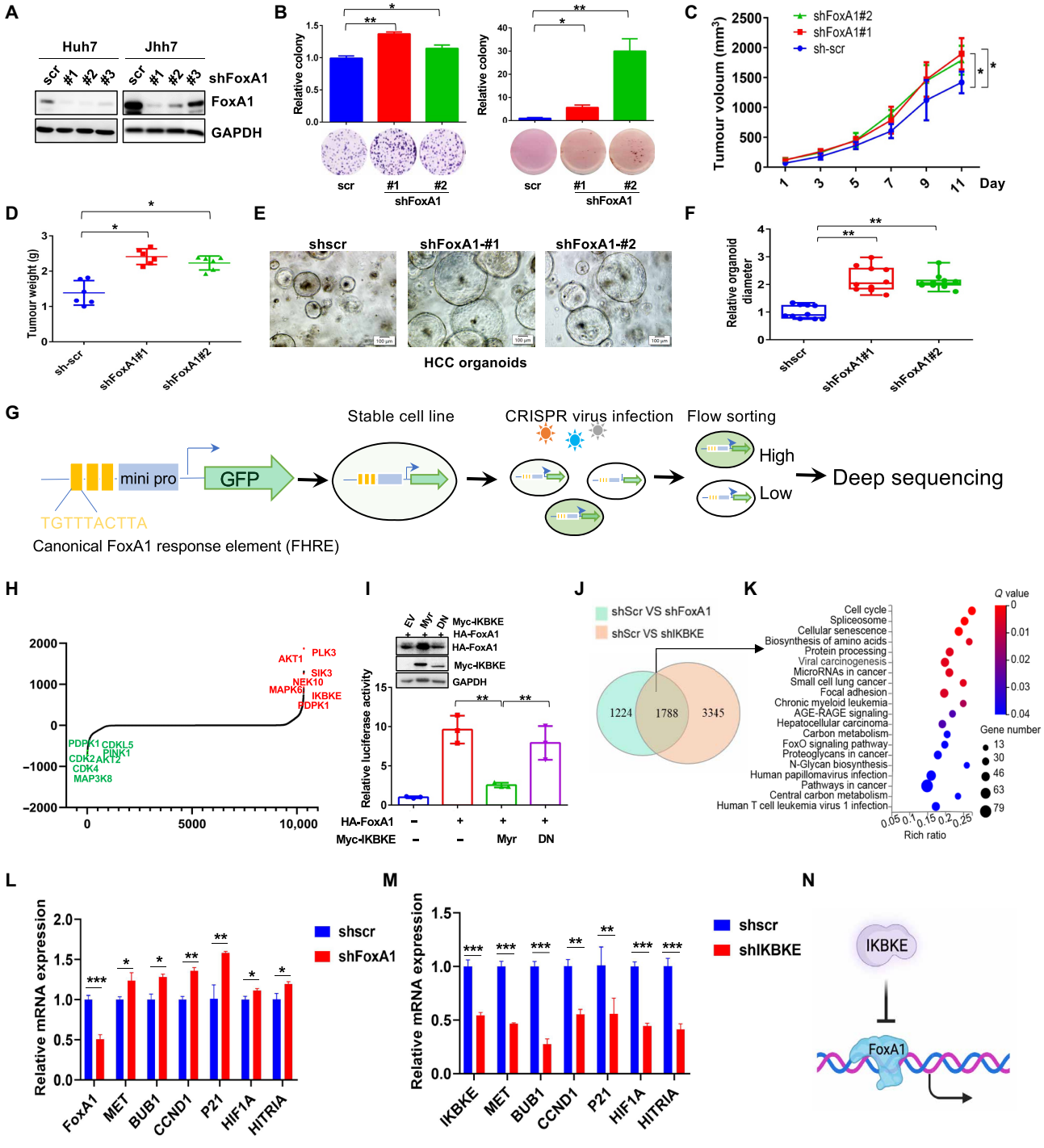

Fig. 1. IKBKE negatively regulates FoxA1 activity and tumor suppressor function. (**A**) Immunoblotting (IB) analysis of whole-cell lysate (WCL) derived from Huh7 and Jhh7 cells infected with short hair RNAs (shRNAs) targeting *FoxA1*. GAPDH, glyceraldehyde-3-phosphate dehydrogenase. (**B**) Huh7 cells generated in (A) were subjected to colony formation and soft agar assays. The relative colony numbers were quantified. Means ± SD, $n = 3$, Student's t test. $^*P < 0.05$ and $^{**}P < 0.01$. (**C** and **D**) Huh7 cells generated in (A) were subjected to xenograft mouse assays. Tumor sizes were monitored (C), and dissected tumors were weighed and calculated (D). Means ± SD, $n = 6$, two-way analysis of variance (ANOVA) test for (C) and Student's t test for (D). $^*P < 0.05$. (**E**) Micrograph shows representative shFoxA1 HCC organoids. Scale bars, 100 μm. (**F**) Box-whisker plot show relative size (diameter) of HCC tumoroids (E). Means ± SD, $n = 10$, Student's t test. $^{**}P < 0.01$. (**G**) Workflow of kinome screening using CRISPR-Cas9 system. (**H**) Scatter plot shows the top candidate single guide RNA (sgRNA) genes of high-throughput sequencing for (G). (**I**) FoxA1 luciferase reporter assays were performed, and the results normalized to level of EV (empty vector) activity. Means ± SD, $n = 3$, Student's t test. $^{**}P < 0.01$. IB analysis of WCL derived from 293T cells transfected with indicated constructs (top). (**J**) Venn diagram indicates the numbers of differentially expressed genes (DEGs) between shFoxA1 and shIKBKE in Huh7 cells. (**K**) Kyoto Encyclopedia of Genes and Genomes (KEGG) Pathway enrichment results of top enriched pathways in crossed genes (J). (**L** and **M**) Quantitative polymerase chain reaction (qPCR) validation of crossed gene from (J) in Huh7 cell lines. (**N**) Schematic model indicates that IKBKE inactivates FoxA1 transcriptional activity.

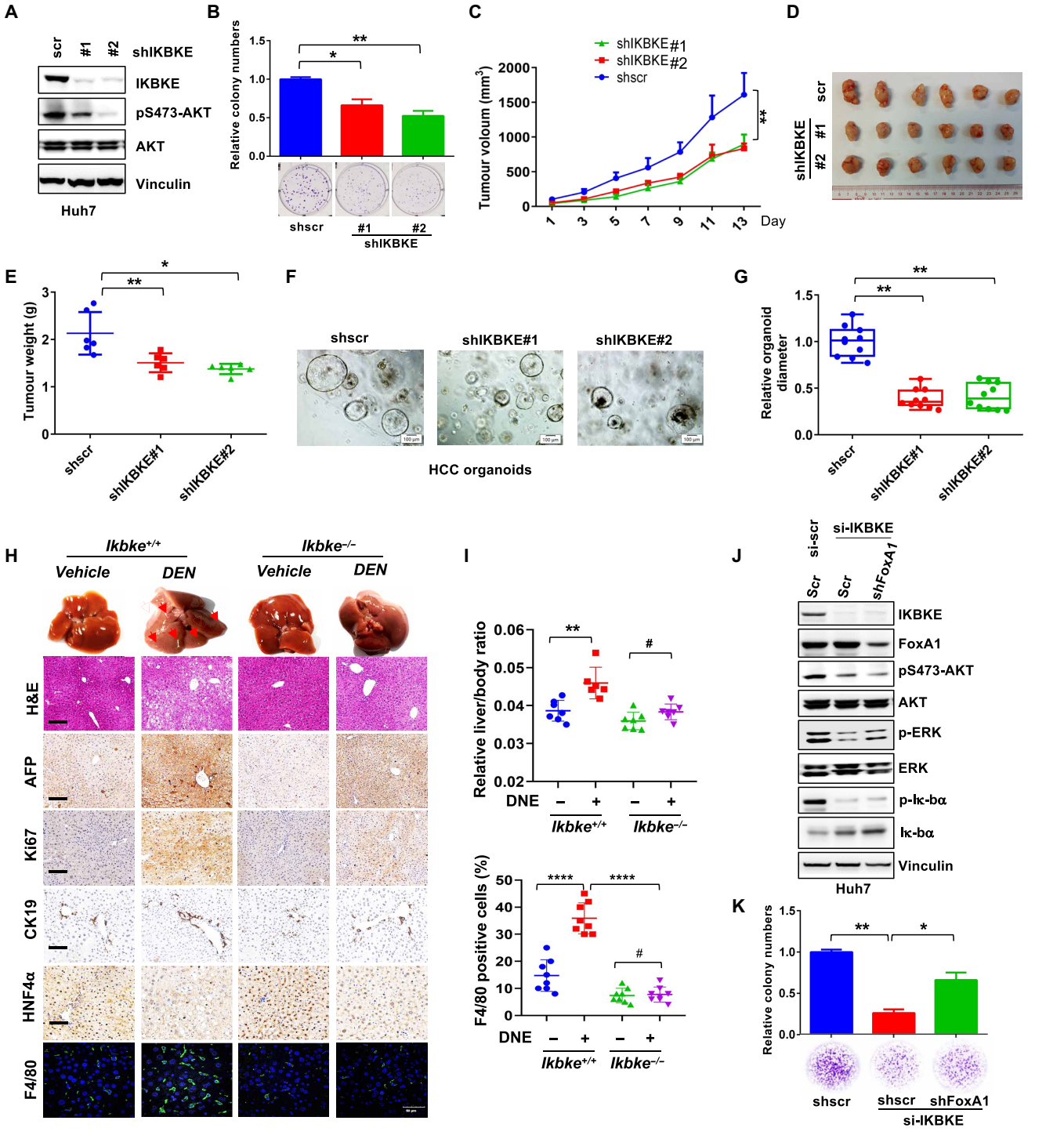

Fig. 2. IKBKE promotes liver tumorigenesis. (**A**) IB analysis of WCL derived from Huh7 cells infected with shRNAs targeting *IKBKE*. (**B**) Cells generated in (A) were subjected to colony formation and soft agar assays. The relative colony numbers were quantified. Means ± SD, $n = 3$, Student's t test. $^{*}P < 0.05$ and $^{**}P < 0.01$. (**C** to **E**) Cells generated in (A) were subjected to xenograft mouse assays. Tumor sizes were monitored (C), and dissected tumors (D) were weighed and calculated (E). Means ± SD, $n = 6$, two-way *ANOVA* test for (C) and Student's t test for (D). $^{*}P < 0.05$ and $^{**}P < 0.01$. (**F**) Micrograph shows representative shIKBKE HCC organoids. Scale bars, 100 μm. (**G**) Box-whisker plot show relative size (diameter) of HCC organoids (F). Means ± SD, $n = 10$, Student's t test. $^{**}P < 0.01$. (**H**) Macroscopic images represent the hematoxylin and eosin (H&E), AFP, Ki67, CK19, and HNF4a staining of WT and *Ikbke*$^{-/-}$ mouse livers treated with or without DEN, and the immunofluorescence (IF) staining of F4/80 was also represented. Scale bars, 100 μm. (**I**) Liver/body ratio was quantified (means ± SD, $n = 6$ or 7, Student's t test) and the F4/80 positive cells were quantified (means ± SD, $n = 8$, Student's t test). $^{**}P < 0.01$ and $^{****}P < 0.0001$; **#** means no significance. (**J** and **K**) Huh7 cells were infected with shRNAs against *FoxA1* and selected with puromycin (1 μg/ml) for 5 days. After that, the resulting Huh7 cells were infected with *IKBKE* small interfering RNA and subjected to IB analysis (J) and colony formation assays [(K) bottom], and the relative colony numbers were quantified (K, top). Means ± SD, $n = 3$, Student's t test. $^{*}P < 0.05$ and $^{**}P < 0.01$.

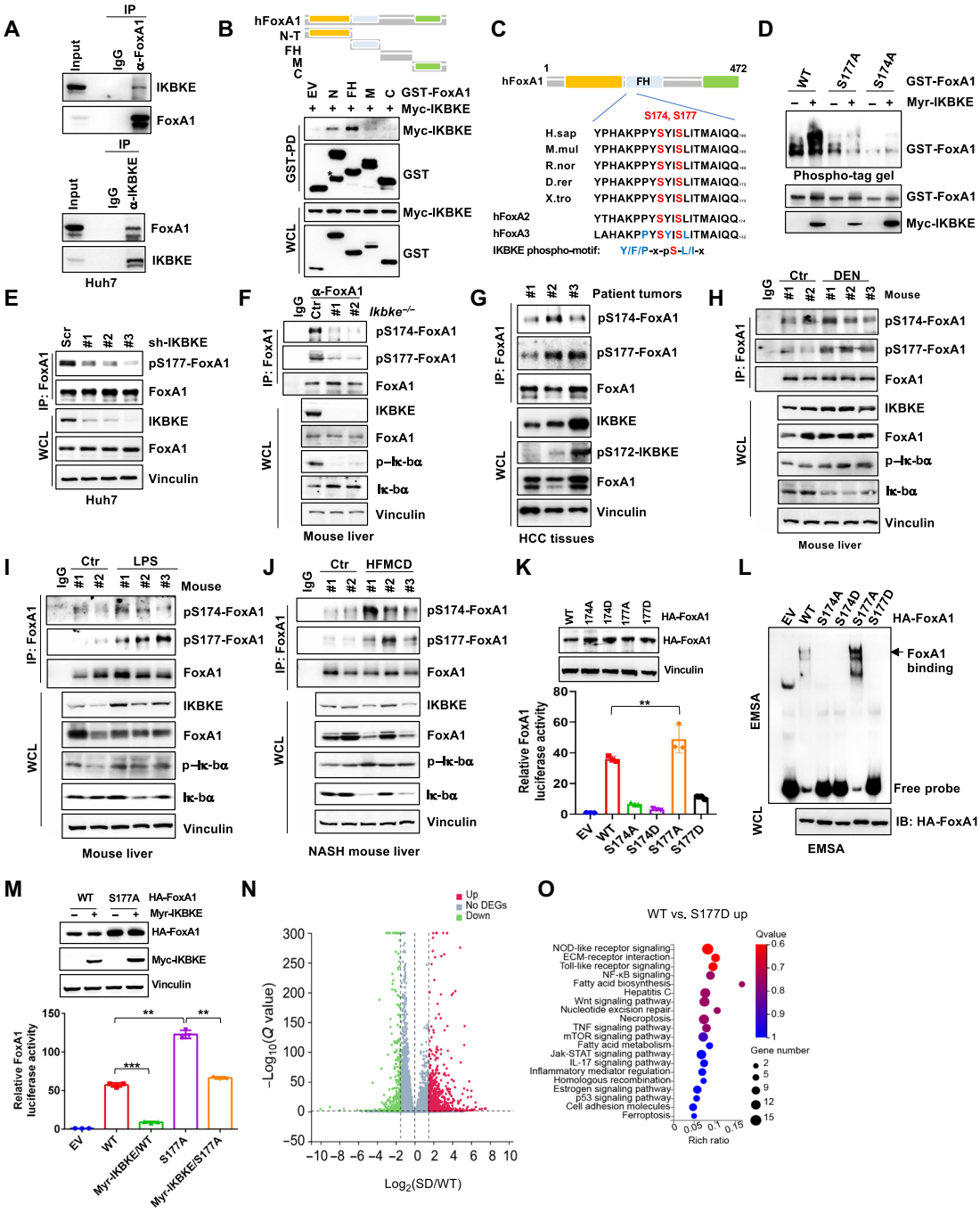

Fig. 3. IKBKE directly phosphorylates FoxA1 to repress its transcriptional activity. (**A**) IB analysis of WCL and immunoprecipitation (IP) products derived from Huh7 cells. Immunoglobulin G (IgG) was used as negative control. (**B**) Functional domain of full-length hFoxA1 and its different truncated constructions are represented and subjected for IB analysis. (**C**) A schematic presentation of the evolutionarily conserved putative IKBKE phosphor-motif in hFoxA1. (**D**) Phospho-tag SDS–polyacrylamide gel electrophoresis (SDS-PAGE) IB analysis of WCL derived from 293T cells transfected with indicated constructs. (**E** to **G**) IB analysis of WCL and IP products derived from Huh7 cells infected with indicated shRNAs (E) or from *Ikbke*$^{-/-}$ and counterpart mice (F), as well as patients with HCC (G). Scr, sh-scramble RNA. (**H**) C57/BL6 male mice were gavage-administrated by DEN (100 mg/kg) for 48 hours with equal volume of 0.9% saline as control. The mouse livers were harvested for IB analysis. (**I**) LPS (10 mg/kg) was intraperitoneally injected into C57/BL6 male mice for 6 hours with equal volume of PBS as the control. The mouse livers were harvested for IB analysis. (**J**) Nonalcoholic steatohepatitis (NASH) mouse model was established by feeding C57/BL6 male mice with high fat methionine-choline deficient diet (HFMCD) (A06071301, Research Diets) for 6 weeks. The mouse livers were harvested for IB analysis. (**K** and **M**) Luciferase reporter assays were performed in 293T cells transfected indicated constructs (as IB analysis of top), and the reporter results were normalized to the level of EV activity. Means ± SD, $n = 3$, Student's t test. $^{**}P < 0.01$ and $^{***}P < 0.001$. (**L**) Electrophoretic mobility shift assay (EMSA) was performed with cell lysates from 293T cells transfected with indicated constructs. EV, as a negative control. (**N**) Volcano plot represents the DEGs in Huh7 shFoxA1 cells stabilized with WT- and S177D-FoxA1. (**O**) KEGG pathway enrichment results of top enriched pathways were obtained from Huh7 shFoxA1 cells stabilized with WT- and S177D-FoxA1. mTOR, mammalian target of rapamycin; ECM, extracellular matrix.

phosphorylated (Fig. 3C and fig. S5, D and E). Notably, both S174 and S177 are evolutionally conserved in the FoxA subfamily and different species, as well as in some members of the Fox family (Fig. 3C). S174 and S177 also share a conserved IKBKE phosphorylation motif defined in previously established substrates such as cylindromatosis (CYLD) (Fig. 3C) (*16*, *34*). To validate these phosphorylation events, we performed phospho-tag assays and observed that both S174A and S177A mutant markedly reduced IKBKE-mediated band shifts in FoxA1 (Fig. 3D and fig. S5F). Subsequently, we developed specific antibodies against phosphorylated FoxA1-S174 and S177, respectively (fig. S5G), and observed that WT or Myr-IKBKE but not DN-IKBKE promoted FoxA1 phosphorylation both under physiological conditions (fig. S5, H to K) and in vitro kinase assay (fig. S5L). However, FoxA2 displayed a relatively low phosphorylation (fig. S5M), possibly due to its lower binding affinity to IKBKE (fig. S4H). IKBKE-mediated phosphorylation of FoxA1 was detected at endogenous levels both in HCC cells, human HCC specimens, and murine liver tissues treated by DEN, LPS, or high-fat diet (Fig. 3, E to J), suggesting that FoxA1 is a bona fide substrate of IKBKE.

IKBKE represses FoxA1 transcriptional activity in a phosphorylation-dependent manner

To investigate the effect of IKBKE-mediated phosphorylation on FoxA1 transcriptional activity, the nonphosphorylated mimetic (S174A and S177A) and phosphorylated mimetic (S174D and S177D) FoxA1 mutants were generated, in contrast to ectopic expression of IKBKE or S177D-FoxA1, S177A mutant FoxA1 resulted in enhanced FoxA1 binding to the corresponding DNA elements and elevated its transcriptional activity (Fig. 3, K and L, and fig. S6A). Notably, S177A mutation-induced FoxA1 transcriptional activity could only be lesser reduced compared with WT-FoxA1 upon ectopic expression of IKBKE (Fig. 3M).

Next, compared with WT, the S177D mutant transcriptionally altered the downstream target genes of FoxA1 (Fig. 3, N and O, and fig. S6, B and C). Unexpectedly, both S174A and S174D exhibited similar phenotypes to impair FoxA1 binding to DNA elements and inhibit FoxA1 transcriptional activity (Fig. 3, K and L, and fig. S6A). To point out this distinction, we analyzed the localization of S174 and S177 sites in FoxA1, and observed that S174, but not S177, resides at a critical position for FoxA1 binding to DNA (fig. S6D). Therefore, replacement of S174 with either Ala (S174A) or Asp (S174D) might alter the conformation of FoxA1, thereby interfering its DNA binding properties. Therefore, although S174 also undergoes IKBKE-mediated phosphorylation (Fig. 3C), we could not use S174A or S174D mutation to mimic (non)-phosphorylated S174, as usually done in the phosphorylation study. Therefore, in this study, we mainly focused on IKBKE-mediated phosphorylation of FoxA1 at S177 to inhibit its function.

IKBKE dissembles FoxA1 complex formation

Consistent with the previous finding that FoxA1 formed a dimer and integrated with cofactors into a large complex to carry out its transcriptional function (*35*), we observed that FoxA1 formed homodimer with its FH domain (fig. S6E). Ectopic expression of IKBKE or S177D-FoxA1 mutant, but not DN-IKBKE or S177A-FoxA1 mutant, markedly blocked FoxA1 dimerization (fig. S6, F and G). Furthermore, both IKBKE expression and the S177D mutant reduced FoxA1 complex formation, whereas the S177A mutant enhanced its complex assembly (Fig. 4, A and B). Specifically, as a physiological partner, GATA binging protein 4 (GATA4) interacts with FoxA1 and plays a key role in its tumor suppressor function in HCC (*24*). Here, we observed that forced expression of IKBKE and the S177D mutant blocked, whereas overexpression of the S177A mutant enhanced GATA4 binding to FoxA1 (Fig. 4, C to E, and fig. S6H). These findings suggest that IKBKE phosphorylates FoxA1 to reduce its transcriptional complex formation (Fig. 4F).

Biologically, S177D enhanced colony formation in cells (Fig. 4, G and H, and fig. S7, A and B) and HCC organoid models compared to WT and S177A-FoxA1 (Fig. 4I). To study the role of phosphorylated S177 in vivo, S177A and S177D-Foxa1 knock-in (designated $Foxa1^{S177A}$ and $Foxa1^{S177D}$) and knockout (designated $Foxa1^{-/-}$) mice were generated (fig. S7, C to E). Among them, both $Foxa1^{S177D}$ and $Foxa1^{-/-}$ displayed potential birth defects compared with intact and corresponding heterogeneous mice, while $Foxa1^{S177A}$ had no obvious effect on mouse birth and growth (fig. S7F). To explored whether the nonphosphomimic FoxA1 (S177A) acts as a tumor suppressor, a hydrodynamic HCC mouse model was used, and the results showed that $Foxa1^{S177A}$ greatly reduced *Myr-Akt1;N-Ras*–induced HCC (Fig. 5A), coupled with reducing fibroblast formation (indicated by Masson), hepatotoxicity [alpha fetoprotein positive (AFP^+)], and inflammation ($F4/80^+$) (Fig. 5, B and C). This result indicates that non-IKBKE phosphorylated FoxA1 (S177A) possibly enhances hepatic tissue differentiation to antagonize tumorigenesis, consistent with our hypothesis that S177A enhances FoxA1 binding to GATA4 to promote hepatic differentiation, as previously reported (*24*).

However, because of the developmental defects of $Foxa1^{S177D}$ mice and technique limitation in generating liver-conditional $Foxa1^{S177D}$ knock-in mice, it was not possible to assess whether $Foxa1^{S177D}$ mice are prone to liver tumorigenesis. Alternatively, we harvested 5- to 12-day-old $Foxa1^{S177D}$ and counterpart WT ($Foxa1^{WT}$) mice and observed that $Foxa1^{S177D}$ mice phenocopied $Foxa1^{-/-}$ mice exhibiting marked growth retardation of body and organs (fig. S7, G and H). Consistent with the previous finding that *Gata4* deficiency leads to hypoplastic liver in mice and thus affects liver development (*24*), $Foxa1^{S177D}$ mice also largely reduced mouse liver development and suppressed it by enhancing liver injury (AFP^+) and inflammation ($F4/80^+$) (Fig. 5, D to F), accompanied by impaired hepatocyte cycle and inflammation (Fig. 5, G and H, and fig. S7, I to L). Together, these findings demonstrate that IKBKE inhibits FoxA1 transcriptional activity and tumor suppression in a phosphorylation-dependent manner.

IKBKE inhibitor alleviates liver tumorigenesis

Although only 4 to 8% of *IKBKE* amplifications were identified in HCC by IHC staining, we identified IKBKE high expression in at least 60% patients with HCC (figs. S1K and S3, D and E). Because HCC is often present under inflammatory conditions, we also observed that DEN, a typical carcinogen that induces HCC, could enhance the expression of Ikbke in mouse liver tissues (fig. S7M), which was consistent with the above finding that $Ikbke^{-/-}$ reduced DEN-induced liver injury and inflammation compared with intact mice (Fig. 2, H and I, and fig. S4D). Because IKBKE has been identified as highly expressed and plays an important pathological role in HCC, we tended to verify the efficacy of IKBKE inhibitors as potential therapies for HCC. To this end, the IKBKE inhibitor compound 1 (COMPD1) was used (*36*), which substantially inhibited the IKBKE-induced band shift and phosphorylation of FoxA1 (fig. S8, A to C). Furthermore, this inhibitor also markedly rescued the decreased

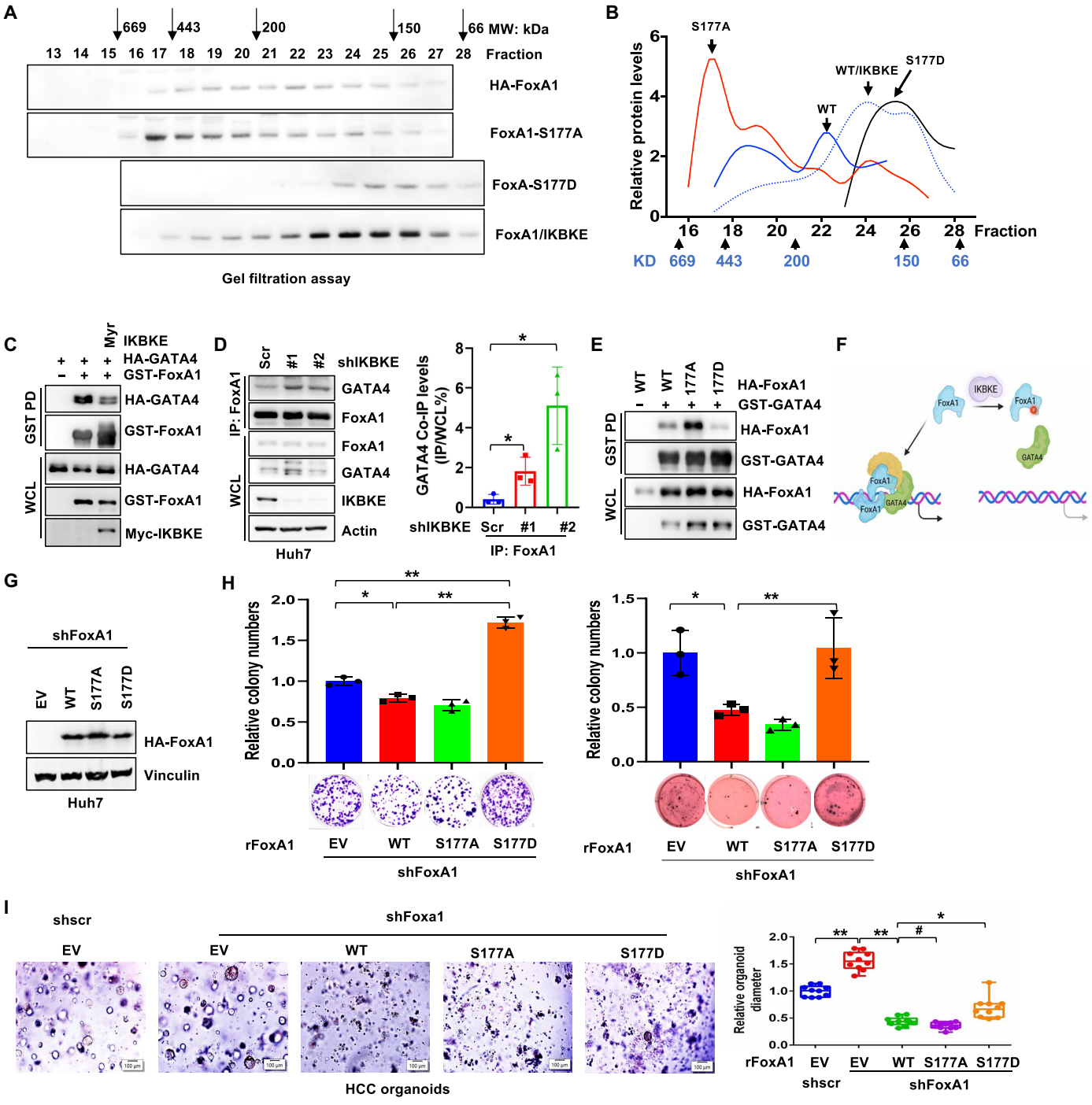

Fig. 4. IKBKE phosphorylates FoxA1 to disassemble its complex formation. (**A** and **B**) IB analysis of gel filtration products derived from 293T cells transfected with indicted constructions (A). MW, molecular weight. The quantitative trendline results of protein expression levels were quantified by Image J software (B). (**C** and **E**) IB analysis of WCL and GST–pull-down products derived from 293T cells transfected with indicated constructs. (**D**) IB analysis of WCL and IP products derived from Huh7 cells infected with indicated shRNAs. Scr, sh-scramble RNA, as a negative control. The GATA4 co-IP levels were quantified. Means ± SD, $n = 3$, Student's t test. $^*P < 0.05$. (**F**) Schematic model indicates that IKBKE could directly phosphorylate FoxA1 to repress its binding with GATA4. (**G** and **H**) Huh7 cells were infected with shRNAs against *FoxA1* and selected with puromycin for 5 days, and the resulting cells were infected with virus encoding different mutants of FoxA1 and selected with hygromycin for 5 days. Then, the cells were subjected to IB analysis (G), colony formation, and soft agar assays (H). The relative colony numbers were quantified. Means ± SD, $n = 3$, Student's t test. $^*P < 0.05$ and $^{**}P < 0.01$. (**I**) *FoxA1*-deleted (shFoxA1) HCC organoids were infected with virus encoding different mutants of FoxA1 and selected with hygromycin for 5 days. Micrograph shows the resulting HCC organoids. Scale bars, 100 μm (I). Box-whisker plot show relative size (diameter) of HCC tumoroids. Means ± SD, $n = 10$, Student's t test. $^*P < 0.05$ and $^{**}P < 0.01$.

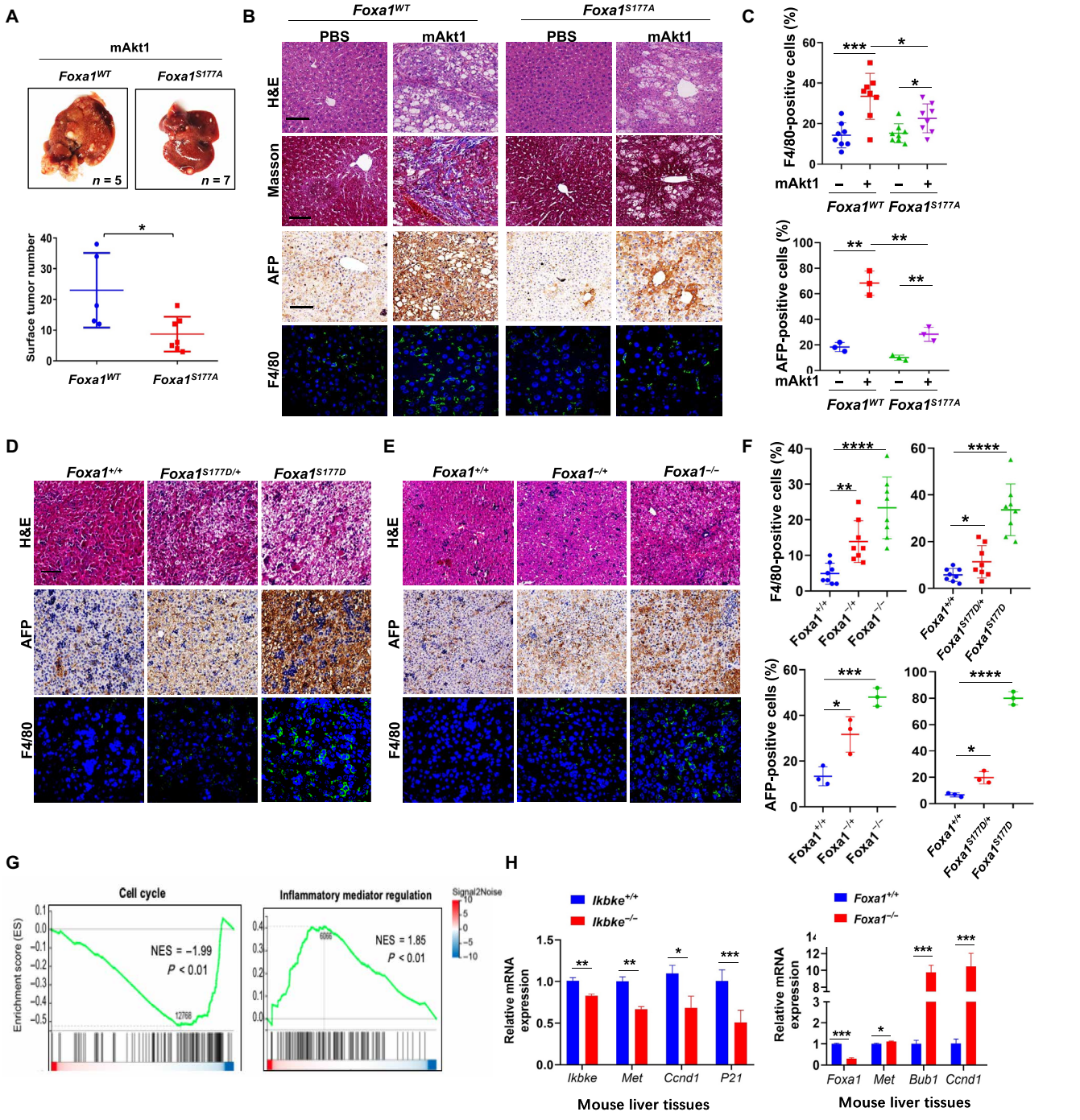

Fig. 5. Phosphorylation of FoxA1 represses its tumor suppressor roles. (**A** to **C**) Macroscopic liver images of WT and S177A-KI mice with indicated treatment. Control group mice were tail vein injected with empty vector in 2 ml of saline solution, while *Myr-mAKT1;N-Ras-V12;transposase* constructs were injected in test groups (A). Also, the surface tumors were calculated (A). Means ± SD, Student's *t* test. **P* < 0.05. Macroscopic liver images represented the H&E and Masson staining of WT and *Foxa1*$^{S177A/S177A}$ mice (scale bar, 2 mm) and the AFP and F4/80 IHC staining results of WT and *Foxa1*$^{S177A/S177A}$ mice (scale bars, 2 mm and 100 μm) (B). The F4/80- and AFP-positive cells were quantified (C). Means ± SD, *n* = 8 for F4/80 and *n* = 3 for AFP, Student's *t* test. **P* < 0.05 and ****P* < 0.001. (**D** to **F**) Macroscopic liver images represent the H&E staining of *Foxa1*$^{+/+}$(WT), *Foxa1*$^{S177D/+}$(Het), *Foxa1*^{S177D} (Homo), *Foxa1*$^{+/-}$ and *Foxa1*$^{-/-}$ mice, and the AFP and F4/80 IHC staining (D and E). Scale bars, 100 μm. The F4/80- and AFP-positive cells were quantified (F). Means ± SD, *n* = 8 for F4/80 and *n* = 3 for AFP, Student's *t* test. **P* < 0.05, ***P* < 0.01, ****P* < 0.001, and *****P* < 0.0001. (**G**) Gene Set Enrichment Analysis of DGEs in (fig. S7I). The genes sorted along the horizontal axis corresponded to the running enrichment score at vertical axis. In the vertical axis, a positive value indicates enrichment at the top, the left genes of the peak genes are core genes, and the negative values indicate the opposite. In the horizontal axis, the red and blue heatmap means the genes expression abundance arrangement. The dark red means a larger log fold change (logFC), and dark blue means a smaller logFC. (**H**) qPCR validation of crossed gene from (Fig. 1J) in *Ikbke* and *Foxa1* knockout mouse liver tissues, respectively. Means ± SD, *n* = 3, Student's *t* test. **P* < 0.05, ***P* < 0.01, and ****P* < 0.001. NES, normalized enrichment score.

FoxA1 transcriptional activity by IKBKE (Fig. 6A). In addition, COMPD1 not only restored the interaction of FoxA1 with its partner GATA4 (Fig. 6, B and C), but also rescued its protein complex formation (fig. S8D). Functionally, COMPD1 potently suppressed HCC growth both in cells and in vivo (Fig. 6, D to G, and fig. S8, E to H), while enhancing apoptosis (Fig. 6, F and G). COMPD1 decreased intact but with a lesser extent of *FoxA1*-depleted, liver cancer cell growth (Fig. 6, D to G, and fig. S8F), suggesting that IKBKE partially regulates HCC by inactivating FoxA1. To further evaluate the potential antitumor role of COMPD1 in liver tumorigenesis in vivo, a C-Myc–driven HCC mouse model was used (*37*). After COMPD1 administration (Fig. 6H), we observed a significant attenuation of C-Myc–induced HCC with reduced FoxA1 phosphorylation compared with the vehicle-treated group (Fig. 6, I to J), along with decreased liver injury (AFP^+), inflammation ($F4/80^+$), proliferation ($Ki67^+$), and increased apoptosis (cleaved Caspase 3) (Fig. 6, K and L, and fig. S8I). These observations together suggest that targeting IKBKE will effectively inhibit liver tumorigenesis, in part, by unleashing FoxA1 tumor suppressor function (Fig. 7).

DISCUSSION

Frequent mutations of *FoxA1* are strongly associated with breast and prostate tumorigenesis (*20*, *21*, *38*); however, genetic alterations of *FoxA1* rarely occur in other tumors including liver cancer, suggesting that FoxA1 may play distinct roles in these cancer settings. Initially, FoxA1 has been identified in rat liver tissues and plays an important role in hepatocyte differentiation and maturation (*35*, *39*). For that, a liver conditional *Foxa1/2* double knockout mouse models were generated and displayed a sex-dependent distinct function in DEN-induced HCC (*22*). Mutations in *Gata4*, a binding cofactor of FoxA1, could enhance liver tumorigenesis, and the FoxA1-lysine demethylase 6A (KDM6A)–Rho GDP dissociation inhibitor beta (ARHGDIB) axis can also suppress the malignancy of bladder cancer (*23*, *24*); thus, we hypothesized that FoxA1 might play a tumor suppressor role in HCC. Here, we disclosed FoxA1 as a tumor suppressor in HCC, although high FoxA1 expression was observed in HCC tissues and associated with poor survival that are consistent with previous studies (*26, 27*). The different findings of FoxA1 in prostate/breast cancer versus liver cancer may be due to the fact that FoxA1 regulates distinct downstream genes by cooperating with different cofactors. Thus, although genes in the transcriptional regulation of FoxA1 between ER^+ breast cancer and AR^+ prostate cancer overlapped, the differences in the overlap between FoxA1 as a tumor suppressor and oncogene need to be further explored.

IKBKE has been recognized as an oncogene in a variety of tumors, including breast and lung cancers. Besides activating the NF-κB pathway, IKBKE could also directly phosphorylate AKT and IRF3, thus, we commonly used phosphorylation of Iκ-Bα with p-IRF3 or p-AKT to reflect the activation of IKBKE. Here, we find that IKBKE inhibits FoxA1 transcriptional activity in a phosphorylation-dependent manner and exerts oncogenic roles in HCC, possibly through unleashing FoxA1-mediated negative regulation of cell cycle–associated genes (such as BUB, CCND1, and MET). At the same time, a question is raised, how does IKBKE regulate FoxA1 to perform oncogenic functions once FoxA1 acts as an oncogene in breast/prostate cancer? We postulate that IKBKE may regulate FoxA1 transcriptional profiles by selectively altering its interaction with cofactors. Because of bearing similar phosphorylation motifs, FoxA2 and FoxA3 also undergo IKBKE-mediated phosphorylation, but with different trends. Due to the redundant and identical roles and tissue-context distribution of FoxA1-3, whether IKBKE can regulate cellular biology and pathological functions by phosphorylating FoxA2/3, especially in liver tumorigenesis, deserves further study. Accumulating substrates of IKBKE have also recently been identified to affect inflammation and immune pathways. Although we have preliminarily elucidated FoxA1 as the major downstream effector of IKBKE in HCC, more in vivo studies are needed by using $Foxa1^{S177A}$ knock-in mice, including DEN-induced HCC models and crossing with C-Myc–driven HCC mouse models.

As an inducible inflammation kinase, IKBKE is thought to be induced by diverse physiological or pathological stimuli, including PMA, TNFα, and LPS. These cytokines or chemokines have been shown to play pivotal roles in liver tumorigenesis (*40*). Because HCC is mainly induced by hepatis virus and metabolic mediators, we hypothesize that IKBKE might be induced/activated under these different conditions by inhibiting the tumor suppressor FoxA1, thereby promoting liver tumorigenesis. We observe that DEN challenge can also enhance IKBKE expression in mice, accompanied with FoxA1 phosphorylation. LPS administration and high-fat diet feeding could also promote NF-κB activation and IKBKE-mediated FoxA1 phosphorylation (Fig. 3, I and J), suggesting the potential function of IKBKE-FoxA1 axis in promoting HCC. However, although we validated that DEN-induced HCC is IKBKE dependent, whether LPS- and high-fat–induced liver damage and HCC are IKBKE activity dependent that, particularly via FoxA1 phosphorylation, are worth further investigations. Meanwhile, although viral infections have been disclosed to activate IKBKE (*41*), because HBV/HCV could not infect mouse hepatocyte, we only postulate that this virus-induced IKBKE activation may result in FoxA1 inactivation and liver tumorigenesis. Together, our findings suggest that under conditions of *IKBKE* amplification/activation genetically or stimulated with inflammation/carcinogens, FoxA1 undergoes IKBKE-mediated phosphorylation, which abolishes its transcriptional activity and tumor suppressor function, thus leading to HCC. We also highlight the strategy to combat HCC with IKBKE-specific inhibitors.

MATERIALS AND METHODS

Cell culture, transfection, fractionations, and viral infection

Huh7, Jhh7, PLC/PRF5, HepG2, SK-HEP-1, SNU739, and 293T cells were obtained from American Type Culture Collection and maintained in Dulbecco's modified Eagle's medium (DMEM); Li7, SNU761, and SNU387 cells were maintained in RPMI 1640 medium containing 10% fetal bovine serum (Gibco), penicillin (100 U/ml), and streptomycin (100 μg/ml; Gibco). Cells transfected with Lipofectamine (Invitrogen) or Polyethylenimine [(PEI) Polysciences] were performed according to the manufacturer's instructions. Cell fractionations were performed with the Cell Fractionation Kit (CST9038). IKBKE inhibitors COMPD1 (C1) was obtained from Selleck (S8922).

For generating knockout/knockdown or reconstituted expressing cells, human embryonic kidney–293 T cells were used for packaging of lentiviral viruses. After transfection 48 and 72 hours, supernatant was harvested and filtered through a 0.45-μm syringe filter and used to infect cells in the presence of polybrene (4 μg/ml). Infected cells were selected using hygromycin B (200 μg/ml) or puromycin (1 μg/ml) for 5 days.

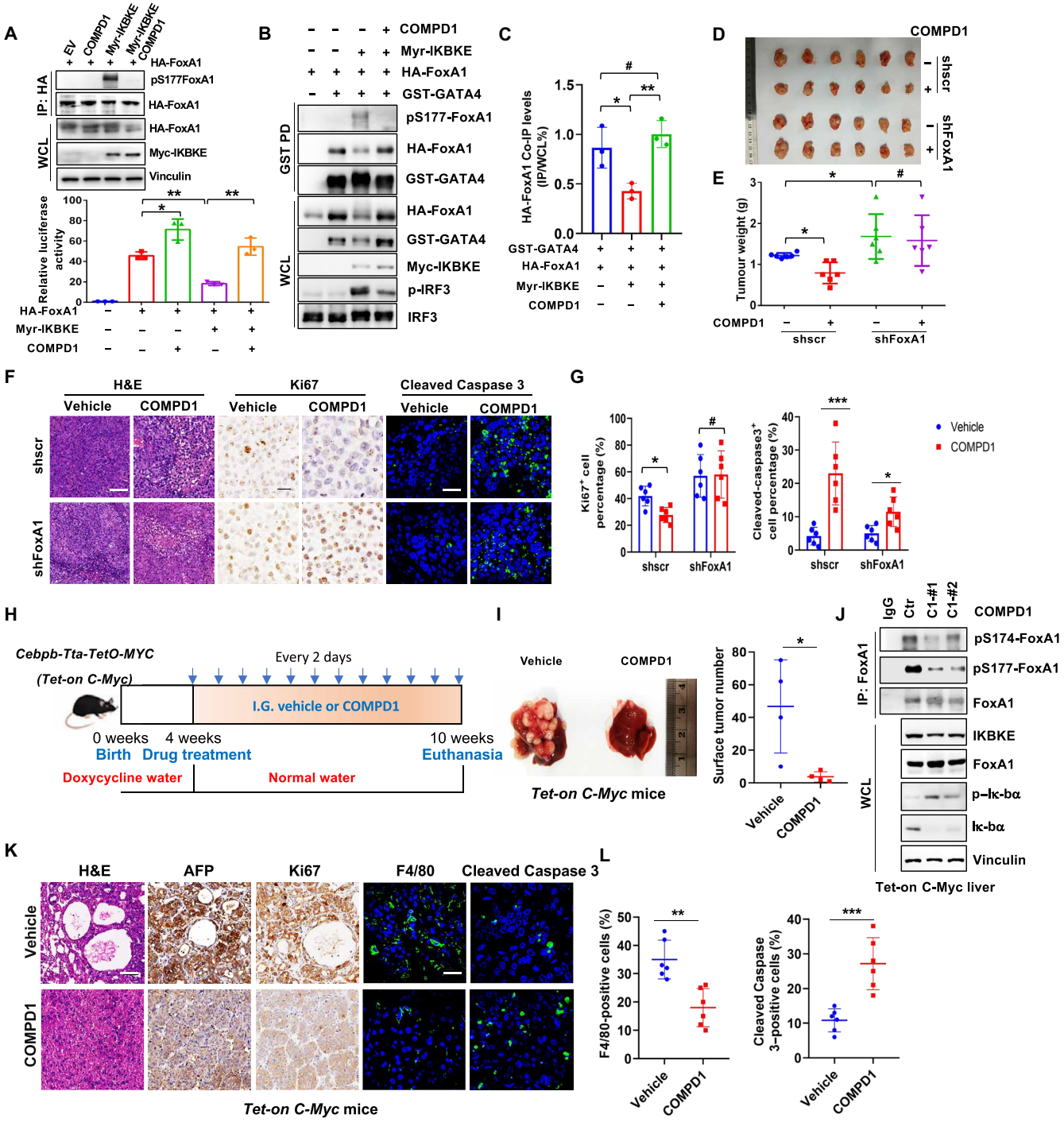

Fig. 6. IKBKE inhibitor represses tumor growth partially by recovering FoxA1 activity. (**A**) Reporter assays were performed in 293T cells transfected indicated constructs treated with/without COMPD1 (5 μM for 4 hours), and the results were normalized to EV activity. Means ± SD, $n = 3$, Student's t test. $^{*}P < 0.05$ and $^{**}P < 0.01$. (**B** and **C**) IB analysis of WCL and GST–pull-down products from 293T cells transfected indicated constructs and treated with/without COMPD1 (5 μM for 4 hours). HA-FoxA1 co-IP levels were quantified. Means ± SD, $n = 3$, Student's t test. $^{*}P < 0.05$ and $^{**}P < 0.01$. (**D** to **G**) Huh7 cells were infected with shRNAs against *FoxA1*, selected with puromycin for 5 days, and then subjected to xenograft assays treated with/without COMPD1 [intragastrical administration (IG) with 30 mg/kg per 2 days]. Tumors were dissected (D) and weighed (E). Data were shown as means ± SD, $n = 6$, Student's t test. $^{*}P < 0.05$. Ki67 staining and cleaved Caspase 3 staining were quantified [(F) and (G)] (means ± SD, $n = 6$, Student's t test). $^{*}P < 0.05$ and $^{***}P < 0.001$. (**H**) Illustration of the flow for treating *Cebpb-Tta-TetO-Myc* mice with IKBKE inhibitor. Briefly, male mice were terminated with doxycycline water (100 μg/ml) at age 4 weeks and then administrated with COMPD1 (I.G. 30 mg/kg) or vehicle every 2 days for 6 weeks. (**I** to **L**) Macroscopic liver images of *C-Myc* mice with/without COMPD1 treatment. The surface tumors were calculated (I). Means ± SD, $n = 4$, Student's t test. $^{*}P < 0.05$. The mouse livers were harvested for IB analysis (J). The H&E, AFP, Ki67, F4/80, and cleaved Caspase 3 staining were represented (K). The F4/80 and cleaved Caspase3–positive cells were quantified (L). Means ± SD, $n = 6$, Student's t test. $^{**}P < 0.01$ and $^{***}P < 0.001$. Scale bars, 2 mm for H&E and IHC and 100 μm for IF.

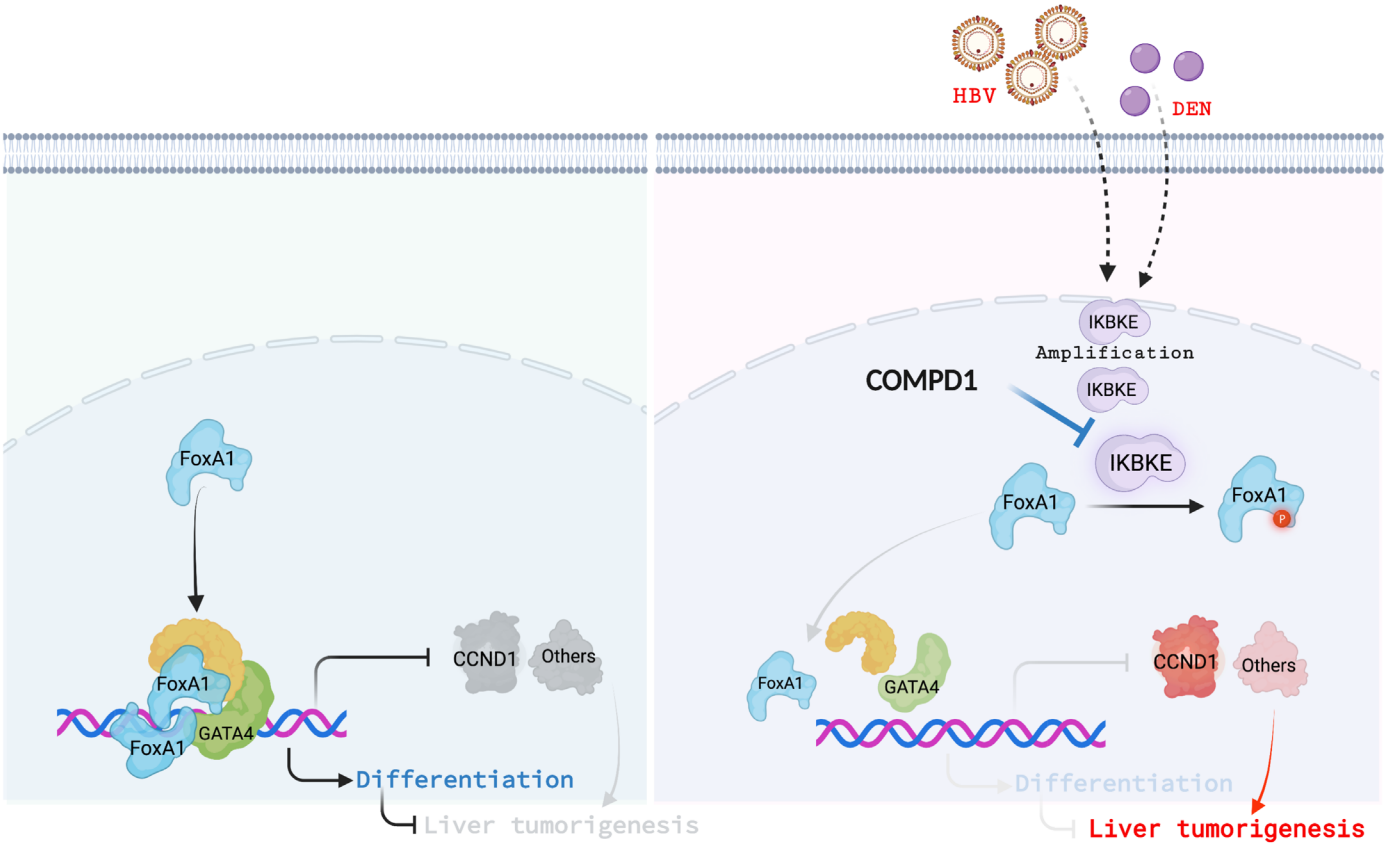

Fig. 7. Illustration of the IKBKE-FoxA1 axis in liver tumorigenesis. Schematic model indicates that under physiological conditions, FoxA1 forms complex with GATA4 to facilitate downstream differentiation-associated transcriptional regulation in repressing tumorigenesis; on the other hand, elevated IKBKE induced by virus infection or DEN administration could phosphorylate FoxA1 to reduce its complex formation, leading to inactivation of FoxA1 and promotion of tumorigenesis, highlighting the potential role of IKBKE inhibitor for liver cancer therapies. The figure was generated with Biorender.com.

Antibodies

All antibodies were diluted in Tris Buffered Saline with Tween-20 (TBST) buffer with 5% nonfat milk for Western blot. Anti-IKBKE antibody (1:3000; 3416 s), anti-FoxA1 antibody (1:3000; 53528 s), anti–TNF receptor–associated factor 2 antibody (1:3000; 4724 s), anti-ubiquitin antibody (1:2000; 3933 s), anti–p–NF-κB antibody (1:3000; 3033 s), anti–C-MYC antibody (1:3000; 18,583 s), anti–extracellular signal–regulated kinase 1/2 (ERK1/2) antibody (1:3000; 4695 s), anti-ERK1/2-p antibody (1:3000; 4370 s), anti–Iκ-Bα antibody (1:3000; 4812 s), anti–p–Iκ-Bα antibody (1:3000; 2859 s), anti-IRF3 antibody (1:3000; 4302 s), anti–p–IRF-3 antibody (1:3000; 37829 s), anti–cleaved Caspase 3 antibody (1:50; 9664 s), anti-AKT1 antibody (1:3000; 75692 s), anti-pSer^{473}-AKT antibody (1:3000; 4060), anti–Myc-tag antibody (1:3000; 2276 s), and anti–glutathione *S*-transferase (GST)–tag antibody (1:3000; 2625 s) were obtained from Cell Signaling Technology (CST). Anti-p65 antibody (1:2000; 10745-1-AP), anti–GST-tag antibody (1:2000; 66001-2-lgl), anti-AFP antibody (1:100 14550-1-AP), F4/80 antibody (1:1000; 28463-1-AP) were obtained from Proteintech. Anti–thiophosphate ester antibody (1:3000; ab92570) were obtained from Abcam. Polyclonal anti-FoxA1 antibody (1:100; EA32402) was obtained from ELGBIO. Anti-Ki67 antibody (1:100; GB111499) was obtained from Servicebio. Anti- IKKE antibody (1:200;VMA00517) was obtained from Bio-Rad. Polyclonal anti–hemagglutinin (HA) antibody (1:1000; sc-805) was obtained from Santa Cruz Biotechnology. Polyclonal anti-Flag antibody (1:1000; F-2425), monoclonal anti-Flag antibody (1:3000; F-3165, clone M2), anti-tubulin antibody (1:3000; T-5168), anti-vinculin antibody (1:3000; V4505), anti-HA agarose beads (A-2095), peroxidase-conjugated anti-mouse secondary antibody (A-4416), and peroxidase-conjugated anti-rabbit secondary antibody (A-4914) were obtained from Sigma-Aldrich. Mouse anti-rabbit immunoglobulin G LCS (1:10,000; A25022) was obtained from Abbkine. Glutathione Sepharose 4B (17-0756-05) was obtained from GE Healthcare, Monoclonal anti-HA antibody (1:3000; 901503), anti–glyceraldehyde-3-phosphate dehydrogenase (1:3000; 649201) antibody was obtained from BioLegend.

The polyclonal phosphorylation antibodies against pS174 and pS177-FoxA1 (1:1000) generated by Abclonal Technology were derived from rabbit. The antigen sequence used for immunization was FoxA1 amino acids 170 to 177 (KPPY**S**YIS) for pS174 and amino acids 174 to 180 (C-SYI**S**LIT) for pS177 (**S** stands for phosphorylated residue in this synthetic peptide). The antibodies were affinity purified using the antigen peptide column and counter-selected with unmodified antigen.

Plasmid construction

To create pCMV-GST-FoxA1-FL (GST-FoxA1) and pCDNA3-HA-FoxA1 (HA-FoxA1), rat and human FoxA1 cDNA was cloned into the

Bam H1 and SaI 1 sites of pCMV-GST-vector and pCDNA3-HA-vector, respectively. CMV-GST-FoxA1-N, CMV-GST-FoxA1-FH, CMV-GST-FoxA1-M, and CMV-GST-FoxA1-C were cloned into the mammalian expression GST-fusion vectors. HA-FoxA1-S177A and HA-FoxA1-S177D constructs were generated by site-directed mutagenesis using overlap extension polymerase chain reaction (PCR). All primers and short hair RNA (shRNA)/single guide RNA (sgRNA) sequences were listed in table S1. pLenti-HA-Hygro-FoxA1, pLenti-HA-Hygro-FoxA1-S177A, and pLenti-HA-Hygro-FoxA1-S177D were cloned into the mammalian expression pLenti-HA-Hygro vectors. Various FoxA1, IKBKE mutants were generated by site-directed mutagenesis using overlap extension PCR. All mutants were verified by DNA sequencing.

Human primary HCC cancer organoid culture and HCC organoid generation

Human primary HCC organoids (L231T) were generated and cultured in three-dimensional Matrigel using DMEM/F12 medium with 1% GlutaMAX, 10 mM Hepes, 1:50 B27 supplement, 1:100 N2 supplement, 1.25 mM *N*-acetyl-L-cysteine, 10% (v/v) Rspo-1–conditioned medium, 30% (v/v) Wnt3a-conditioned medium, 10 μM nicotinamide, 10 nM recombinant human (Leu^{15})–gastrin I, recombinant human EGF (50 ng/ml), recombinant human FGF10 (100 ng/ml), recombinant human hepatocyte growth factor [(HGF) 25 ng/ml], 10 μM forskolin, 5 μM A8301, Noggin (25 ng/ml) ,10 μM Y27632, and 1% penicillin/streptomycin. To knockdown *FoxA1* and *IKBKE*, organoids were digested into single-cell suspension and infected with lentiviral shRNAs for 6 hours at 37°C and harvested at centrifugation (500*g*) followed by resuspension in Matrigel. Also, packaging of cDNA expressing viruses were infected for sh-FoxA1 organoids. Constructed organoids were maintained in the presence of hygromycin (200 μg/ml) or puromycin (1 μg/ml) depending on the viral vectors.

Immunoprecipitation and immunoblotting analyses

To immunoprecipitate ectopically expressed HA-tagged and GST-tagged proteins, transfected cells were lysed 48 hours after transfection in EBC buffer [50 mM tris (pH 7.5), 120 mM NaCl, and 0.5% NP-40] supplemented with protease inhibitors (cOmplete Mini, Roche) and phosphatase inhibitors (PhosSTOP, Roche). The whole-cell lysates were immunoprecipitated with distinct agarose beads for HA and GST at 4°C for 2 to 4 hours. After three washes with NaCl–EDTA–Tris–NP-40 (NETN) buffer [20 mM tris (pH 8.0), 150 mM NaCl, 1 mM EDTA, and 0.5% NP-40], the bound proteins samples were resolved by SDS–polyacrylamide gel electrophoresis (SDS-PAGE).

Kinome screening

A lentiviral reporter vector pLenti-hygro-CMV-FoxA1-luci-EGFP was used to integrate into 293T cells, and stable clones were obtained after selected with hygromycin. Next, the clones were infected with CRISPR-Cas9 kinase lentivirus library then selected for 7 days with the treatment of puromycin to establish the reporter system. The reporter system cells were subjected to flow cytometry sorting to collect the GFP intensity high and low cells, which further be the preparation of genomic DNA extraction. Also, the CRISPR library sgRNAs were amplified by PCR and aligned to the collected DNA using high-throughput sequencing technology (Novogene). After alignment, the differentially expressed sgRNAs were calculated and the corresponding genes are ranked.

Purification of GST-tagged proteins from bacteria

Recombinant GST-conjugated FoxA1 and mutants were generated by transforming the BL21 (DE3) *Escherichia coli* strain with pGEX-FoxA1-20aa, pGEX-FoxA1-S177A-20aa, pGEX-FoxA1-S174A-20aa, respectively. The cultured bacteria were grown with vigorous shaking at 37°C to an outer diameter of 0.8 and then for 12 to 16 hours at 16°C by adding 0.1 mM isopropyl-β-D-thiogalactopyranoside. Recombinant proteins were purified from harvested pellets and resuspended in 10 ml of EBC buffer for sonication. The supernatant was incubated with 50 μl of 50% glutathione sepharose slurry (Pierce) for 3 hours at 4°C, and the glutathione beads were washed three times with phosphate-buffered saline (PBS) buffer and eluted by elution buffer. Recovery and yield of the desired proteins (or complexes) was confirmed by analyzing 10 μl of beads by Coomassie blue staining and quantified with bovine serum albumin (BSA) standards.

Peptide synthesis and dot immunoblot assays

FoxA1-WT, FoxA1-pS177 and FoxA1-pS174 peptides used for dot blot assays were synthesized by Abclonal. The sequences were listed as: Foxa1-WT: Bio-KRSYPHAKPPYSYISLITMAIQQA, Foxa1-pS177: Bio-KRSYPHAKPPYSYI(pS)LITMAIQQA, and Foxa1-pS174: Bio-KRSYPHAKPPY(pS)YISLITMAIQQA.

Peptides were diluted into 2 mg/ml for further biochemical assays. For dot blot assays, peptides were diluted with PBS and spotted onto nitrocellulose membrane with the amount of 0.01, 0.03, 0.1, 0.3, and 1 μg. The membrane was dried and blocked by soaking in TBST buffer with 5% nonfat milk for immunoblot analysis.

DNA synthesis and pulldown assays

Before harvest the whole cell lysates, the synthesized Bio-5xFRHE DNA fragments were incubated with streptomycin beads 1 hour at room temperature (RT). After 48-hour transfection, the transfected cells were lysed in EBC buffer [50 mM tris (pH 7.5), 120 mM NaCl, and 0.5% NP-40] supplemented with protease inhibitors (cOmplete Protease Inhibitor Cocktail, Roche) and phosphatase inhibitors (PhosSTOP, Roche). The whole-cell lysates were added into the incubated streptomycin beads mixture and incubated at 4°C shaker for 2 to 4 hours. After three washes with NETN buffer, the proteins samples were resolved by SDS-PAGE.

In vitro kinase assay

For kinase assay using GST-tagged proteins from cell lysate as substrate, the GST-FoxA1, GST-FoxA1-S177A and GST-FoxA1-S174A proteins were pulled down by 30 μl Glutathione-sepharose slurry from 293 T cells. The obtained beads were respectively mixed with 10× kinase buffer (CST), 200 μM adenosine 5′-triphosphate (ATP), and 100 ng of adenosine 5′-thiotriphosphate (Abcam) and the ddH_2O and the 70 ng of re-IKBKE (Sigma-Aldrich) were added to reach a 30 μl of kinase reaction system. Kinase reactions were first carried out at 30°C for 30 min and stopped by 1 μl of 3 mM EDTA and next incubated at RT for 2 hours by adding 1.5 μl of 50 mM p-Nitrobenzyl mesylate (PNBM) and lastly stopped by 10 μl of 5× SDS buffer. After reaction, the targeted proteins were resolved by SDS-PAGE. The phosphorylated FoxA1 was detected by specific antibodies.

For kinase assay using purified recombinant GST-conjugated proteins as substrate, the GST-FoxA1-20aa, the GST-FoxA1-S177A-20aa, and the GST-FoxA1-S174A-20aa were added into a 30 μl of kinase reaction system. After reaction, the targeted proteins were resolved by

SDS-PAGE, stained by Coomassie blue and detected by specific antibodies.

Immunofluorescence staining

Cells were transfected with indicated plasmids and grown on glass coverslips, fixed with 4% paraformaldehyde at RT for 15 min, washed three times with PBS, and then permeabilized with 0.05% Triton X-100 at RT for 10 min. Following washed three times with PBS, the coverslips were blocked with 5% BSA for 30 min and then incubated overnight with indicated antibodies at 4°C. Following washing three times with PBST, the coverslips were incubated with secondary antibodies, anti-mouse Alexa Fluor 643 (CST), for 1 hour at room temperature in dark. Following washing three times with PBST, the coverslips were stained with TRITC phalloidin at RT for 30 min and with 4′,6-diamidino-2-phenylindole in the dark and mounted using glycerin. The mounted coverslips were subject to detection with Zeiss LSM880 with Airyscan microscopy.

Liver tissues and IHC staining

The HCC tissue microarray (TMA) was obtained from the First Affiliated Hospital of Sun Yat-sen University. The study was approved by the Cantonal Ethics Committee of Sun Yat-sen University, and informed consent was obtained from each patient. We also combined another HCC tumor tissue microarrays (Biomax, BC03117a) to analyze the clinical relevance of IKBKE in HCC. IHC was performed as previous reported including heat-induced antigen retrieval procedures (*42*). Incubation with antibodies against IKBKE (1:200), Ki67 antibody (1:100), AFP antibody (1:100), cleaved Caspase 3 antibody (1:50), and F4/80 antibody (1:1000) were carried out at 4°C overnight. All stainings were blindly evaluated by two pathologists by quantitative imaging methods; the percentage of immunostaining and the staining intensity were recorded. An *H* score was calculated using the following formula: $H\ \text{score} = \Sigma\ (\text{PI} \times I) =$ (percentage of cells of weak intensity × 1) + (percentage of cells of moderate intensity × 2) + (percentage of cells of strong intensity × 3). PI indicates the percentage of positive cells versus all cells, and *I* represent the staining intensity. The scores over 6 were identified as "high," and the scores less than 6 were identified as "low." In addition, the scores between 6 and 9 were identified as "middle."

Histopathologic analysis

Hematoxylin and eosin staining was performed on paraffin-embedded tissues according to manuscript (Solarbio, catalog no. G1120). Liver fibrosis was assessed via Masson staining (Solarbio, catalog no. G1340). Histopathological images were captured under fully automatic digital pathology slide scanner (kfbio) and analyzed by QuPath software. Images were quantified using ImageJ and GraphPad Prism version 6.0 software.

Dual-luciferase reporter assay

Oligonucleotide fragment containing three tandem fork-head domain (FHKD) consensus (canonical or noncanonical) motifs (*21*) with minor promoters were cloned into pGL3-basic vectors (Promega). The pGL3-3xFoxA1-Luc was transiently transfected using Lipofectamine with PLUS reagents into 293T cells along with Renilla (pRL-SV40-Renilla, Promega) as internal control. Response rations are expressed relative to signal obtained from the empty vector control wells transfected with pCDN3-HA vector. After transfection for 40 hours, the cells were harvested and analyzed with a dual-luciferase reporter assay system (Promega) according to the manufacturer's instructions. All results are means and standard deviating from experiments performed in biological triplicates ($n = 3$).

Electrophoretic mobility shift assay

Biotin end-labeled probe was prepared by SBS Genetech (China). Electrophoretic mobility shift assay (EMSA) was performed using the LightShift Chemiluminescent EMSA Kit (Thermo Fisher Scientific, 20148) according to the manufacturer's instructions. Briefly, DNA binding reactions were performed in 20 μl of system containing biotin-labeled oligonucleotides and nuclear extracts. Additional unlabeled oligonucleotides were added for competition. Reaction products were then separated by nondenaturing polyacrylamide gel electrophoresis. Next, the protein-DNA complexes were transferred onto a positively charged nylon membrane (GE), and the nylon membrane was cross-linking with excitation light (120 mJ/cm^2) for 1.5 min and lastly detected by chemiluminescence.

Gel filtration chromatography analysis

293T cells were separately transfected with indicated plasmids, then washed with PBS, and lysed in 1 ml of EBC buffer. Gel filtration marker kit (Sigma-Aldrich) was used to determine the protein molecular weight corresponding to the number of tubes for further analysis. A total of 1 ml of lysate was loaded onto a 200 increase 10/300 GL column after filtered through a 0.22-μm syringe filter. Chromatography was performed on the AKTA avant 150 with EBC buffer. One column volume of eluates was fractionated with 500 μl in each fraction at the elution speed of 0.8 ml/min. A total of 40-μl aliquots of each fraction were loaded onto SDS-PAGE and detected with indicated antibodies.

Real-time reverse transcriptional PCR and RNA sequencing analyses

Total RNA was extracted using a phenol-chloroform method with TRIzol regent (Takara, 9109), and cDNA was reverse-transcribed using the PrimeScript reverse transcription kit (Takara 6210A) according to the manufacturer's instructions. Real-time PCR was performed using the SYBR Green Premix Pro Taq HS qPCR Kit II (Rox Plus) (AG11719). The primers used are listed in table S1.

High-quality total RNA was used for the preparation of sequencing libraries using the oligo-dT method and the BGISEQ-500 platform (BGI-Shenzhen, China). The sequencing data were filtered with SOAPnuke (v1.5.2) by removing reads containing sequencing adapter; removing reads whose low-quality base ratio (base quality less than or equal to 5) is more than 20%; removing reads whose unknown base ("N" base) ratio is more than 5aaaaa5, afterward, clean reads were obtained and stored in FASTQ format. The clean reads were mapped to the reference genome using the reference coding gene set, and then expression level of gene was calculated by RSEM (v1.1.12). The heatmap was drawn by pheatmap (v1.0.8) according to the gene expression in different samples. Essentially, differential expression analysis was performed using the DESeq2 (v1.4.5) with Q value ≤ 0.05 to take insight to the change of phenotype, Gene Ontology (www.geneontology.org/) and Kyoto Encyclopedia of Genes and Genomes KEGG (www.kegg.jp/) enrichment analysis of annotated different expressed gene was performed by Phyper (http://en.wikipedia.org/wiki/Hypergeometric_distribution) based on hypergeometric test. The significant levels of terms and pathways were corrected by Q value with a rigorous threshold (Q value ≤ 0.05) by Bonferroni.

Mass spectrometry analysis

Gel bands of proteins with catalase activity were excised for in gel digestion, and proteins were identified by mass spectrometry as we previously described (*43*). Briefly, proteins were disulfide reduced with 5 mM dithiothreitol and alkylated with 11 mM iodoacetamide. In-gel digestion was performed using sequencing grade-modified trypsin in 50 mM ammonium bicarbonate at 37°C overnight. The peptides were extracted twice with 1% trifluoroacetic acid in 50% acetonitrile aqueous solution for 1 hour. The peptide extracts were then centrifuged in a SpeedVac to reduce the volume. The peptides were resuspended in 20 μl of 0.1% trifluoroacetic acid, followed by centrifugation at 20,000*g* at 4°C for 15 min to remove any particulate impurities.

For liquid chromatography–tandem mass spectrometry (LC-MS/MS) analysis, peptides were separated by a 40-min gradient elution at a flow rate of 0.300 μl/min with a Thermo-Dionex Ultimate 3000 HPLC system, which was directly interfaced with a Thermo Orbitrap Fusion Lumos mass spectrometer. The analytical column was a homemade fused silica capillary column (75 μm in inner diameter, 150 mm in length; Upchurch, Oak Harbor, WA) packed with C-18 resin (300 A, 5 μm; Varian, Lexington, MA). Mobile phase A was consisted of 0.1% formic acid, and mobile phase B was consisted of 100% acetonitrile and 0.1% formic acid. An LTQ-Orbitrap mass spectrometer was operated in the data-dependent acquisition mode using Byonic software, and there is a single full-scan mass spectrum in the Orbitrap (300 to 1500 mass/charge ratio, 120,000 resolution) followed by 3-s data-dependent MS/MS scans in an ion-routing multipole at 40% normalized high energy collision dissociation (HCD). MS/MS spectra from each LC-MS/MS run were searched against the human database using Proteome Discoverer (version 1.4) searching algorithm. The search criteria were as follows: Full tryptic specificity was required; two missed cleavages were allowed; carbamidomethylation was set as fixed modification; phosphorylation and oxidation (M) were set as variable modifications; precursor ion mass tolerance was 20 parts per million for all MS acquired in the Orbitrap mass analyzer; and fragment ion mass tolerance was 0.8 Da for all MS2 spectra acquired in the LTQ. High confidence score filter (false discovery rate < 1%) was used to select the "hit" peptides, and their corresponding MS/MS spectra were manually inspected.

Colony formation and soft agar assays

Following procedures previously described in (*44*), we seeded cells into six-well plates (300 or 600 cells per well) and left for 12 to 20 days until formation of visible colonies. Colonies were washed with PBS two times and fixed with 10% acetic acid/10% methanol for 1 hour and then stained with 0.4% crystal violet in 20% ethanol for 2 hours. After staining, the plates were washed and air-dried, and colony numbers were counted and quantified. The anchorage-independent cell growth assays were performed as described previously (*45*). Briefly, the assays were preformed using six-well plates where the solid medium consists of two layers. The bottom layer contains 0.8% noble agar and the top layer contains 0.4% agar suspended with 1×10^4 or 3×10^4 cells. A total of 500 μl of complete DMEM medium was added every 7 days to keep the top layer moisture, and 4 weeks later, the cells were stained with iodonitrotetrazolium chloride (1 mg/ml) (Sigma-Aldrich, I10406) for colony visualization and counting.

Animal ethics statement

All animal procedures were authorized by the Institutional Animal Care and Use Committee (IACUC) of Sun Yat-sen University (SYSU) (approval number: SYSU-IACUC-2021-000527).

Hydrodynamic gene delivery

We use sleeping beauty (SB) transposon system to induce hepatocarcinogenesis mouse model (*46*). Four-week-old male mice were hydrodynamic delivered with 20 μg of Myr-Akt1 and 20 μg of N-RasV12 combined with 2.75 μg of SB transposase in 2 ml of saline via tail vein injections within 10 s. Control mice were injected with 20 μg of N-RasV12 and 2.75 μg of SB transposase. Livers were harvested and used for further analysis after 4- to 6-week hydrodynamic transfection.

DEN-induced model of liver cancer

B6.Cg ($Ikbke^{-/-}$)^{tm1Tman} mice were obtained from the Jackson Laboratory. The offspring were genotyped by PCR of genomic DNA derived from tail clippings, and the homozygous mouse were used for the further experiments. These mice were housed in a specific pathogen–free environment. Two-week-old male $Ikbke^{-/-}$ mice were treated with DEN (25 mg/kg in 0.9% saline; Sigma-Aldrich) by intraperitoneal injection to initiate liver tumor formation. Control mice were intraperitoneally injected with 0.9% saline at the same age. Mice were euthanized at the indicated ages, and liver tissues were collected and analyzed.

Xenografted mouse study

Mouse xenograft assays were performed as described previously (*42*). Briefly, 1×10^6 Huh7 cells were injected into the flank of six female mice (SYSU, 4 to 5 weeks of age). COMPD1 is administered by gavage every 2 days at a dose of 30 mg/kg. Tumor size was measured every 3 days with a caliper, and tumor volume was determined with the formals: $L \times W^2 \times 0.5$, where L is the longest diameter and W is the shortest diameter. Nude mice (4 weeks old, male) were acquired from Guangdong Yaokang Biotechnology company.

Generation and validation of Foxa1^{S177A} and Foxa1^{S177D} knock-in mice

The *Foxa1*^{S177A} and *Foxa1*^{S177D} knock in mice were generated using CRISPR-Cas9 technology by the Cyagen Biosciences. To generate *Foxa1* knock-in mice, the gRNAs against *Foxa1*, the donor oligo containing S177A (TCG to GCC) or S177D (TCG to GAT) mutation, silent mutations (TCC to AGT, CTC to CTG), and Cas9 were co-injected into fertilized mouse eggs to generate targeted knock-in offspring. F0 founder animal was identified by PCR, followed by sequencing analysis or Bcl l restriction analysis. For $Foxa1^{-/-}$ mice, using CRISPR-Cas9 technology to delete 2 base pair in mouse genome, and the offspring were identified by PCR followed by sequencing analysis. These mice were housed in a specific pathogen–free environment. All experimental procedures were approved by the IACUC (RN150D) at SYSU. The research projects that are approved by the IACUC are operated according the applicable institutional regulations. The institute is committed to the highest ethical standards of care for animals used for the purpose of continued progress in the field of human cancer research.

Spontaneous liver cancer model with COMPD1 treatment

The B6.Cg-Tg (*Cebpb-Tta*) 5Bjd/J mice and FVB/N-Tg (tetO-*MYC)* 36aBop/J mice were obtained from the Jackson Laboratory. The

offspring were genotyped by PCR of genomic DNA derived from tail clippings, and the right genotyped mice (*Cebpb*-Tta-TetO-*MYC* model) were used to establish spontaneous liver cancer model. These mice were housed in a specific pathogen–free environment. Three- to 4-week-old *Cebpb-Tta-TetO-MYC* male mice were gavage-treated with COMPD1 [30 mg/kg per 2 days in 0.5% *O*-carboxymethylcellulose (CMC)–Na]. Control mice were gavage-treated with 0.5% CMC-Na at the same age. Mice were euthanized at the indicated ages, and liver tissues were collected and analyzed.

Quantification and statistical analyses

GraphPad Prism version 6.0 was used for statistical analyses. The differences between experimental groups were tested by Student's *t* test or one-way analysis of variance (ANOVA) test. Two-way ANOVA was also applied in the experiments involved with treatment and time course. The difference of IKBKE expression in liver tissues was analyzed with chi-squared (χ^2) test. For mice, tumor formation analysis was carried out by Kaplan-Meier curve analysis (log-rank test at <0.05). For in vivo tumor experiments and IHC staining, data collection and analysis such as tumor measuring were performed by researchers who were blinded to group information. No blinding was involved in other experiments such as Western blot. The threshold for statistical significance was set to $P < 0.05$. Number of n and additional statistical tests can be found in the figure legends.

Supplementary Materials

This PDF file includes:

Figs. S1 to S8

REFERENCES AND NOTES

1. F. Bray, J. Ferlay, I. Soerjomataram, R. L. Siegel, L. A. Torre, A. Jemal, Global cancer statistics 2018: GLOBOCAN estimates of incidence and mortality worldwide for 36 cancers in 185 countries. *CA Cancer J. Clin.* **68**, 394–424 (2018).
2. J. M. Llovet, R. K. Kelley, A. Villanueva, A. G. Singal, E. Pikarsky, S. Roayaie, R. Lencioni, K. Koike, J. Zucman-Rossi, R. S. Finn, Hepatocellular carcinoma. *Nat. Rev. Dis. Primers* **7**, 6 (2021).
3. D. Q. Huang, H. B. El-Serag, R. Loomba, Global epidemiology of NAFLD-related HCC: Trends, predictions, risk factors and prevention. *Nat. Rev. Gastroenterol. Hepatol.* **18**, 223–238 (2021).
4. Q. Zhou, W. Tian, Z. Jiang, T. Huang, C. Ge, T. Liu, F. Zhao, T. Chen, Y. Cui, H. Li, M. Yao, J. Li, H. Tian, A positive feedback loop of AKR1C3-mediated activation of NF-κB and STAT3 facilitates proliferation and metastasis in hepatocellular carcinoma. *Cancer Res.* **81**, 1361–1374 (2021).
5. G. He, M. Karin, NF-κB and STAT3 - key players in liver inflammation and cancer. *Cell Res.* **21**, 159–168 (2011).
6. W. E. Naugler, T. Sakurai, S. Kim, S. Maeda, K. Kim, A. M. Elsharkawy, M. Karin, Gender disparity in liver cancer due to sex differences in MyD88-dependent IL-6 production. *Science* **317**, 121–124 (2007).
7. G. He, G.-Y. Yu, V. Temkin, H. Ogata, C. Kuntzen, T. Sakurai, W. Sieghart, M. Peck-Radosavljevic, H. L. Leffert, M. Karin, Hepatocyte IKKbeta/NF-kappaB inhibits tumor promotion and progression by preventing oxidative stress-driven STAT3 activation. *Cancer Cell* **17**, 286–297 (2010).
8. Y. Sunami, M. Ringelhan, E. Kokai, M. Lu, T. O'Connor, A. Lorentzen, A. Weber, A.-K. Rodewald, B. Müllhaupt, L. Terracciano, S. Gul, S. Wissel, F. Leithäuser, D. Krappmann, P. Riedl, D. Hartmann, R. Schirmbeck, P. Strnad, N. Hüser, J. Kleeff, H. Friess, R. M. Schmid, F. Geisler, T. Wirth, M. Heikenwalder, Canonical NF-κB signaling in hepatocytes acts as a tumor-suppressor in hepatitis B virus surface antigen-driven hepatocellular carcinoma by controlling the unfolded protein response. *Hepatology* **63**, 1592–1607 (2016).
9. Q. He, X. Xia, K. Yao, J. Zeng, W. Wang, Q. Wu, R. Tang, X. Zou, Amlexanox reversed non-alcoholic fatty liver disease through IKKε inhibition of hepatic stellate cell. *Life Sci.* **239**, 117010 (2019).
10. H. Guan, H. Zhang, J. Cai, J. Wu, J. Yuan, J. Li, Z. Huang, M. Li, IKBKE is over-expressed in glioma and contributes to resistance of glioma cells to apoptosis via activating NF-κB. *J. Pathol.* **223**, 436–445 (2011).
11. K. A. Fitzgerald, S. M. McWhirter, K. L. Faia, D. C. Rowe, E. Latz, D. T. Golenbock, A. J. Coyle, S.-M. Liao, T. Maniatis, IKKepsilon and TBK1 are essential components of the IRF3 signaling pathway. *Nat. Immunol.* **4**, 491–496 (2003).
12. T. U. Barbie, G. Alexe, A. R. Aref, S. Li, Z. Zhu, X. Zhang, Y. Imamura, T. C. Thai, Y. Huang, M. Bowden, J. Herndon, T. J. Cohoon, T. Fleming, P. Tamayo, J. P. Mesirov, S. Ogino, K.-K. Wong, M. J. Ellis, W. C. Hahn, D. A. Barbie, W. E. Gillanders, Targeting an IKBKE cytokine network impairs triple-negative breast cancer growth. *J. Clin. Invest.* **124**, 5411–5423 (2014).
13. S. Wang, F. Xie, F. Chu, Z. Zhang, B. Yang, T. Dai, L. Gao, L. Wang, L. Ling, J. Jia, H. van Dam, J. Jin, L. Zhang, F. Zhou, YAP antagonizes innate antiviral immunity and is targeted for lysosomal degradation through IKKε-mediated phosphorylation. *Nat. Immunol.* **18**, 733–743 (2017).
14. D. Zhou, C. Conrad, F. Xia, J.-S. Park, B. Payer, Y. Yin, G. Y. Lauwers, W. Thasler, J. T. Lee, J. Avruch, N. Bardeesy, Mst1 and Mst2 maintain hepatocyte quiescence and suppress hepatocellular carcinoma development through inactivation of the Yap1 oncogene. *Cancer Cell* **16**, 425–438 (2009).
15. K. Brennan, C. Lyons, P. Fernandes, S. Doyle, A. Houston, E. Brint, Engagement of Fas differentially regulates the production of LPS-induced proinflammatory cytokines and type I interferons. *FEBS J.* **286**, 523–535 (2019).
16. R. T. Peters, S. M. Liao, T. Maniatis, IKKepsilon is part of a novel PMA-inducible IkappaB kinase complex. *Mol. Cell* **5**, 513–522 (2000).
17. K. H. Kaestner, J. Katz, Y. Liu, D. J. Drucker, G. Schütz, Inactivation of the winged helix transcription factor *HNF3α* affects glucose homeostasis and islet glucagon gene expression in vivo. *Genes Dev.* **13**, 495–504 (1999).
18. A. Arruabarrena-Aristorena, J. L. V. Maag, S. Kittane, Y. Cai, W. R. Karthaus, E. Ladewig, J. Park, S. Kannan, L. Ferrando, E. Cocco, S. Y. Ho, D. S. Tan, M. Sallaku, F. Wu, B. Acevedo, P. Selenica, D. S. Ross, M. Witkin, C. L. Sawyers, J. S. Reis-Filho, C. S. Verma, R. Jauch, R. Koche, J. Baselga, P. Razavi, E. Toska, M. Scaltriti, FOXA1 mutations reveal distinct chromatin profiles and influence therapeutic response in breast cancer. *Cancer Cell* **38**, 534–550.e9 (2020).
19. S. Gao, S. Chen, D. Han, D. Barrett, W. Han, M. Ahmed, S. Patalano, J. A. Macoska, H. H. He, C. Cai, Forkhead domain mutations in FOXA1 drive prostate cancer progression. *Cell Res.* **29**, 770–772 (2019).
20. S. E. Glont, I. Chernukhin, J. S. Carroll, Comprehensive genomic analysis reveals that the pioneering function of FOXA1 is independent of hormonal signaling. *Cell Rep.* **26**, 2558–2565.e3 (2019).
21. E. J. Adams, W. R. Karthaus, E. Hoover, D. Liu, A. Gruet, Z. Zhang, H. Cho, R. D. Loreto, S. Chhangawala, Y. Liu, P. A. Watson, E. Davicioni, A. Sboner, C. E. Barbieri, R. Bose, C. S. Leslie, C. L. Sawyers, FOXA1 mutations alter pioneering activity, differentiation and prostate cancer phenotypes. *Nature* **571**, 408–412 (2019).
22. Z. Li, G. Tuteja, J. Schug, K. H. Kaestner, Foxa1 and Foxa2 are essential for sexual dimorphism in liver cancer. *Cell* **148**, 72–83 (2012).
23. L. Liu, J. Cui, Y. Zhao, X. Liu, L. Chen, Y. Xia, Y. Wang, S. Chen, S. Sun, B. Shi, Y. Zou, KDM6A-ARHGDIB axis blocks metastasis of bladder cancer by inhibiting Rac1. *Mol. Cancer* **20**, 77 (2021).
24. F. O. Enane, W. H. Shuen, X. Gu, E. Quteba, B. Przychodzen, H. Makishima, J. Bodo, J. Ng, C. L. Chee, R. Ba, L. S. Koh, J. Lim, R. Cheong, M. Teo, Z. Hu, K. P. Ng, J. Maciejewski, T. Radivoyevitch, A. Chung, L. L. Ooi, Y. M. Tan, P.-C. Cheow, P. Chow, C. Y. Chan, K. H. Lim, L. Yerian, E. Hsi, H. C. Toh, Y. Saunthararajah, GATA4 loss of function in liver cancer impedes precursor to hepatocyte transition. *J. Clin. Invest.* **127**, 3527–3542 (2017).
25. S. He, J. Zhang, W. Zhang, F. Chen, R. Luo, FOXA1 inhibits hepatocellular carcinoma progression by suppressing PIK3R1 expression in male patients. *J. Exp. Clin. Cancer Res.* **36**, 175 (2017).
26. Y. Wang, L. Yang, T. Chen, X. Liu, Y. Guo, Q. Zhu, X. Tong, W. Yang, Q. Xu, D. Huang, K. Tu, A novel lncRNA MCM3AP-AS1 promotes the growth of hepatocellular carcinoma by targeting miR-194-5p/FOXA1 axis. *Mol. Cancer* **18**, 28 (2019).
27. Z. Yuan, M. Ye, J. Qie, T. Ye, FOXA1 promotes cell proliferation and suppresses apoptosis in HCC by directly regulating miR-212-3p/FOXA1/AGR2 signaling pathway. *Onco. Targets. Ther.* **13**, 5231–5240 (2020).
28. S. H. Park, K.-W. Fong, J. Kim, F. Wang, X. Lu, Y. Lee, L. T. Brea, K. Wadosky, C. Guo, S. A. Abdulkadir, J. D. Crispino, D. Fang, P. Ntziachristos, X. Liu, X. Li, Y. Wan, D. W. Goodrich, J. C. Zhao, J. Yu, Posttranslational regulation of FOXA1 by Polycomb and BUB3/USP7 deubiquitin complex in prostate cancer. *Sci. Adv.* **7**, eabe2261 (2021).
29. S. Gao, S. Chen, D. Han, Z. Wang, M. Li, W. Han, A. Besschetnova, M. Liu, F. Zhou, D. Barrett, M. P. Luong, J. Owiredu, Y. Liang, M. Ahmed, J. Petricca, S. Patalano, J. A. Macoska, E. Corey, S. Chen, S. P. Balk, H. H. He, C. Cai, Chromatin binding of FOXA1 is promoted by LSD1-mediated demethylation in prostate cancer. *Nat. Genet.* **52**, 1011–1017 (2020).
30. L. Wang, M. Xu, C.-Y. Kao, S. Y. Tsai, M.-J. Tsai, Small molecule JQ1 promotes prostate cancer invasion via BET-independent inactivation of FOXA1. *J. Clin. Invest.* **130**, 1782–1792 (2020).
31. Y. Wu, L. Zhou, Z. Wang, X. Wang, R. Zhang, L. Zheng, T. Kang, Systematic screening for potential therapeutic targets in osteosarcoma through a kinome-wide CRISPR-Cas9 library. *Cancer Biol. Med.* **17**, 782–794 (2020).

32. W. Xie, Q. Jiang, X. Wu, L. Wang, B. Gao, Z. Sun, X. Zhang, L. Bu, Y. Lin, Q. Huang, J. Li, J. Guo, IKBKE phosphorylates and stabilizes Snail to promote breast cancer invasion and metastasis. *Cell Death Differ.* **29**, 1528–1540 (2022).
33. A. Bainbridge, S. Walker, J. Smith, K. Patterson, A. Dutt, Y. M. Ng, H. D. Thomas, L. Wilson, B. M. Cullough, D. Jones, A. Maan, P. Banks, S. R. McCracken, L. Gaughan, C. N. Robson, K. Coffey, IKBKE activity enhances AR levels in advanced prostate cancer via modulation of the Hippo pathway. *Nucleic Acids Res.* **48**, 5366–5382 (2020).
34. W. Reiley, M. Zhang, X. Wu, E. Granger, S.-C. Sun, Regulation of the deubiquitinating enzyme CYLD by IkappaB kinase gamma-dependent phosphorylation. *Mol. Cell. Biol.* **25**, 3886–3895 (2005).
35. G. M. Bernardo, R. A. Keri, FOXA1: A transcription factor with parallel functions in development and cancer. *Biosci. Rep.* **32**, 113–130 (2012).
36. R. W. Jenkins, A. R. Aref, P. H. Lizotte, E. Ivanova, S. Stinson, C. W. Zhou, M. Bowden, J. Deng, H. Liu, D. Miao, M. X. He, W. Walker, G. Zhang, T. Tian, C. Cheng, Z. Wei, S. Palakurthi, M. Bittinger, H. Vitzthum, J. W. Kim, A. Merlino, M. Quinn, C. Venkataramani, J. A. Kaplan, A. Portell, P. C. Gokhale, B. Phillips, A. Smart, A. Rotem, R. E. Jones, L. Keogh, M. Anguiano, L. Stapleton, Z. Jia, M. Barzily-Rokni, I. Cañadas, T. C. Thai, M. R. Hammond, R. Vlahos, E. S. Wang, H. Zhang, S. Li, G. J. Hanna, W. Huang, M. P. Hoang, A. Piris, J.-P. Eliane, A. O. Stemmer-Rachamimov, L. Cameron, M.-J. Su, P. Shah, B. Izar, M. Thakuria, N. R. Le Boeuf, G. Rabinowits, V. Gunda, S. Parangi, J. M. Cleary, B. C. Miller, S. Kitajima, R. Thummalapalli, B. Miao, T. U. Barbie, V. Sivathanu, J. Wong, W. G. Richards, R. Bueno, C. H. Yoon, J. Miret, M. Herlyn, L. A. Garraway, E. M. Van Allen, G. J. Freeman, P. T. Kirschmeier, J. H. Lorch, P. A. Ott, F. S. Hodi, K. T. Flaherty, R. D. Kamm, G. M. Boland, K.-K. Wong, D. Dornan, C. P. Paweletz, D. A. Barbie, Ex vivo profiling of PD-1 blockade using organotypic tumor spheroids. *Cancer Discov.* **8**, 196–215 (2018).
37. M. Jechlinger, K. Podsypanina, H. Varmus, Regulation of transgenes in three-dimensional cultures of primary mouse mammary cells demonstrates oncogene dependence and identifies cells that survive deinduction. *Genes Dev.* **23**, 1677–1688 (2009).
38. S. Wang, S. Singh, M. Katika, S. Lopez-Aviles, A. Hurtado, High throughput chemical screening reveals multiple regulatory proteins on FOXA1 in breast cancer cell lines. *Int. J. Mol. Sci.* **19**, 4123 (2018).
39. E. Lai, V. R. Prezioso, E. Smith, O. Litvin, R. H. Costa, J. E. Darnell Jr., HNF-3A, a hepatocyte-enriched transcription factor of novel structure is regulated transcriptionally. *Genes Dev.* **4**, 1427–1436 (1990).
40. J. Prieto, Inflammation, HCC and sex: IL-6 in the centre of the triangle. *J. Hepatol.* **48**, 380–381 (2008).
41. K. Ohata, T. Ichikawa, K. Nakao, M. Shigeno, D. Nishimura, H. Ishikawa, K. Hamasaki, K. Eguchi, Interferon alpha inhibits the nuclear factor kappa B activation triggered by X gene product of hepatitis B virus in human hepatoma cells. *FEBS Lett.* **553**, 304–308 (2003).
42. Q. Jiang, N. Zheng, L. Bu, X. Zhang, X. Zhang, Y. Wu, Y. Su, L. Wang, X. Zhang, S. Ren, X. Dai, D. Wu, W. Xie, W. Wei, Y. Zhu, J. Guo, SPOP-mediated ubiquitination and degradation of PDK1 suppresses AKT kinase activity and oncogenic functions. *Mol. Cancer* **20**, 100 (2021).
43. Q. Jiang, X. Zhang, X. Dai, S. Han, X. Wu, L. Wang, W. Wei, N. Zhang, W. Xie, J. Guo, S6K1-mediated phosphorylation of PDK1 impairs AKT kinase activity and oncogenic functions. *Nat. Commun.* **13**, 1548 (2022).
44. X. Zhang, Q. Jiang, Y. Su, L. Bu, Z. Sun, X. Wu, B. Gao, L. Wang, Y. Lin, W. Xie, J. Guo, AMPK phosphorylates and stabilises copper transporter 1 to synergise metformin and copper chelator for breast cancer therapy. *Br. J. Cancer* **128**, 1452–1465 (2023).
45. J. Guo, X. Dai, B. Laurent, N. Zheng, W. Gan, J. Zhang, A. Guo, M. Yuan, P. Liu, J. M. Asara, A. Toker, Y. Shi, P. P. Pandolfi, W. Wei, AKT methylation by SETDB1 promotes AKT kinase activity and oncogenic functions. *Nat. Cell Biol.* **21**, 226–237 (2019).
46. Z. Chen, W. Zhu, S. Zhu, K. Sun, J. Liao, H. Liu, Z. Dai, H. Han, X. Ren, Q. Yang, S. Zheng, B. Peng, S. Peng, M. Kuang, S. Lin, METTL1 promotes hepatocarcinogenesis via m^7G tRNA modification-dependent translation control. *Clin. Transl. Med.* **11**, e661 (2021).

Acknowledgments: We thank members of the J.G. laboratory for critical reading and kind suggestions of the manuscript. We thank X. Tian and H. Deng in Center of Protein Analysis Technology, Tsinghua University for MS analysis. **Funding:** This work was supported by the National Key Research and Development Program of China 2023YFC3402100 (to J.G.) and National Natural Science Foundation of China 32070767 (to J.G.). **Author contributions:** Conceptualization: J.G. Methodology: B.G., X.W., L.B., Q.J., X.L., and J.L. Investigation: B.G., X.W., L.B., and Q.J. Visualization: B.G., X.W., L.W., H.L., X.Z., and Y.W. Material support: Y.L., L.X., X.L., and Y.W. Supervision: J.G., W.X., Y.L., and L.X. Writing—original draft: J.G., B.G., and W.X. Writing—review and editing: J.G., W.X., B.G., Y.L., and L.X. **Competing interests:** The authors declare that they have no competing interests. **Data and materials availability:** RNA sequencing data have been deposited in NCBI Sequence Read Archive (SRA) with accession number PRJNA1062288. All data needed to evaluate the conclusions in the paper are present in the paper and/or the Supplementary Materials.

Submitted 9 August 2023
Accepted 8 January 2024
Published 7 February 2024
10.1126/sciadv.adk2285